CONCEPTUAL DESIGN, VALIDATION, AND OPTIMIZATION OF AN ACTIVE MATERIAL ACTUATED BI-STABLE GRIPPING MECHANISM FOR DRONE PERCHING AND RECHARGING

A Thesis

by

JOSEPH ELIE EL-ASHKAR

Submitted to the Graduate and Professional School of
Texas A&M University
in partial fulfillment of the requirements for the degree of

MASTER OF SCIENCE

Chair of Committee,	Darren Hartl
Committee Members,	Mohammad Naraghi
	John Valasek
	Kiju Lee
Head of Department,	Ivett Leyva

August 2023

Major Subject: Aerospace Engineering

ABSTRACT

The energy density limitations of current battery technologies constrain reconnaissance missions carried out by small unmanned aerial systems (UAS). Even in dangerous environments, limited range requires many UAS to return to base for charging. Such flight profiles can compromise the mission and/or waste valuable resources. This work supports a proposed method to mitigate such constraints by focusing on the development of bi-stable active perching mechanisms that enable UAS recharging via surrounding infrastructure (e.g., power lines), allowing for extended mission range. The proposed bi-stabilty allows UAS to perch without requiring critical electrical energy, avoid reliance on reserve power from depleted batteries by storing and then rapidly recovering elastic strain energy. For repeated perching, gripping mechanisms must include some manner of opening/reset mechanism. Previous and current designs typically use servo motors to reset, which have low energy-to-volume ratios and short life span. To increase energy-to-volume ratio and reliability of the reset mechanism, this work will implement active material actuators to reset the bi-stable perching mechanism.

This research effort addressed homogenization and parameterization across disparate bi-stable gripping mechanism concepts followed by a design of experiment (DOE) study via Latin Hypercube sampling. From the DOE, a design was selected and optimized using an efficient global optimization algorithm to find the optimal solution for low drag and high force bi-stable perching.

DEDICATION

For my fiance, future family, parents, and all my loved ones.

CONTRIBUTORS AND FUNDING SOURCES

Contributors

A special thanks to Dr. Hartl for giving me the opportunity to earn my master's degree while working on such an involved and exciting design problem.

I want to thank Dr. Naraghi for believing in me and guiding me throughout my undergraduate research and in turn my graduate research.

I want to thank the gripper research team, Peter Myers, Bruhuadithya Balaji, Alex Lenhard, and Kishore Yelchuri, for their tireless effort and many contributions to the project.

Funding Sources

This work is supported by DEVCOM Army Research Laboratory (ARL) and would not have been possible without the help of Drs. Frank Gardea and Francis Phillips. I am thankful for their guidance and leadership.

NOMENCLATURE

D	Drag of system
D^I	Induced drag of system
D^P	Profile drag of system
D_{ac}	Drag of aircraft
D^0_{ac}	Reference total drag of the aircraft
D^P_{ac}	Profile drag of aircraft
D_g	Gripper drag
D^P_g	Profile drag of the gripper drag
D^I_g	Induced drag of the gripper drag
$C_{D_{ac}}$	Aircraft total coefficient of drag
C_{D_g}	Gripper total coefficient of drag
q_∞	Gripper Total Coefficient of drag
S_{ac}	Aircraft frontal area
c_d	Profile drag coefficient
$C_{D,i}$	Coefficient of induced drag of the aircraft
C_L	Coefficient of lift
S_w	Surface area of the wing
e_0	Oswald's efficiency factor
AR	Wing aspect ratio
b	Wing span
W_{ac}	Weight of aircraft
W_g	Weight of gripper

K	Beam stiffness
t	Beam thickness
w	Beam width
I	Moment of inertia
E	Elastic Modulus or Young's Modulus
FOTC	Flight of the century
DOE	Design of Experiment
EGO	Efficient Global Optimization
FEA	Finite Element Analysis
FE	Finite Element
LP	Low Profile Model
SJ	Strong Jaw Model
BM	Bi-stable Mechanism Model
TS	Torsion Spring Model
LHS	Latin Hypercube Sampling
SMA	Shape Memory Alloys
QS	Quasi-static
MD	Moderate Dissipation
UAS	Unmanned Aerial System

TABLE OF CONTENTS

Page

LIST OF FIGURES

FIGURE Page

LIST OF TABLES

TABLE Page

1. INTRODUCTION

1.1 Drones, Perching, and Recharging

The number of unmanned aircraft systems, also known as either unmanned aerial vehicles or colloquially as drones, has been growing over the last decade and is projected to surpass the number of manned aircraft systems in future markets [1]. Airframe, propulsion, communications, sensors, and information processing constraints limit the demand of the market and are where the majority of development and research resides [1]. Electrically powered aircraft systems are limited by the energy density of today's battery technology [1] and constrain missions with the frequent need to return to base. This is often a waste of time and puts all involved in the mission at risk. Although, the constraints posed by the general UAS market cover the majority of challenges, the need to return to base has not been eliminated. UAS energy density constraints in military and commercial application examples will be highlighted for this discussion.

In an effort to advance unmanned aircraft technology independently of battery development in the military, groups such as FOTC [1] are researching unmanned aircraft systems that either replace depleted batteries or drop them by means of a second UAS or parachute, respectively. For a reconnaissance mission in foreign territory with imminent threats, disposing of batteries by a second UAS system or by parachute is infeasible. Both techniques involve separating what would have been a large battery into multiple batteries. Without the resources to support a UAS with a second refueling UAS the first solution does not hold. The second method of periodically dropping depleted batteries in flight increases aircraft range by 90% [1]. Although, the increased range is desirable, depleted battery cell disposal will incur cost and still require the need to return to base.

Eliminating return to base via remote recharging provides the lowest mission risk of all known solutions. For this reason along with the many different UAS applications and constraints across all markets, various groups across the world are investigating UAS perching and gripping mechanism designs. Common gripper design characteristics investigated by the research community are high-

force gripping, passive perching, and active material reset mechanisms for cyclical use.

Proposed by researchers in Denmark for maintenance on power lines, this approach utilizes base-independent UAS for extended maintenance deployment [2, 3]. This perching mechanism design concept uses two servo motors to trip the mechanism and grip a power line while an electromagnet locks the two jaw tips together for a firm hold. The drone perches and recharges via overhead power lines in order to remain in service without the need to return to base.

A group of researchers from Colorado State University department of mechanical engineering have designed a bi-stable gripping mechanism for mechanically intelligent and passive perching [4]. Although bi-stability is an advantageous design that allows the gripping mechanism to be independent of wireless communication or distance sensors for tripping and gripping, the reset mechanism is designed for UAS with the ability to vertically take off (e.g., quad-copters). The same trigger designed for bi-stable tripping of the mechanism is also used to reset the mechanism with an upward force produced by purely vertical take off.

In Spain, a group of researchers from GURC Robotics Laboratory at the University of Seville designed a light-weight bio-inspired claw for an ornithopter (flapping-wing aerial system) [5]. Thermally actuated SMA springs are used to design a light-weight actuator for the perching mechanism. Motion of the claw was achieved using a tendon-like system of Kevlar thread connected to the SMA spring. The SMA actuated claw allows the ornithopter to fly from an initial vertically perched position, grasp objects to carry in flight, and drop objects while in flight. However, wireless communication is required in order to grasp/perch and reset the mechanism.

A research group from The University of Auckland, New Zealand approached the design of a gripping mechanism by storing strain energy in a torsion spring for high force gripping [6]. However, due to such high forces, the reset mechanism required is large and heavy. The weight and volume is due to the servo motors needed to power a belt-driven system to reset the mechanism. In addition, distance sensors are required to trip the quick release mechanism for gripping.

A research team from the school of mechanical and automotive engineering at Qingdao University of Technology designed two bio-inspired claw perching mechanisms [7]. Similar to that of

the research team in Spain, the claw is actuated by applying tension to a tendon-like system. Both claw designs proposed use fishing line to actuate the claw. However, one claw design variant uses a pulley-system that connects the various members, while the members of the second variant are connected with a tendon-like elastomer with the fishing line routed through holes in the members themselves.

The current state of the art addresses many common issues constraining the UAS markets via passive perching, compact active material actuators, and strain energy dependant quick release mechanisms. However, prior works do not include considerations for fixed wing UAS, one of the cheapest and most available UAS and therefore a UAS type of great commercial and military interest. Moreover, none of the proposed solutions consider combining the advantages of bi-stability, strain energy dependant quick release mechanisms, and active material actuator reset mechanisms for the same gripper design concept. This work will include four gripper concepts that are each enabled by passive bi-stable gripping coupled with active material actuated reset mechanisms with the intention of designing the mechanism using high energy-to-volume and energy-to-mass ratios. This work considers small fixed wing UAS in the gripping mechanism design.

1.2 Concept of Operations

The proposed solution would allow UAS to remain in the field indefinitely and eliminate the need to return to base. The UAS would simply approach surrounding infrastructure with the bi-stable gripping mechanism ready to perch. In the mission concept depicted in Figure 1.1, the UAS approaches a power line as though it was approaching a landing strip; but instead of approaching a landing strip with landing gear, the UAS approaches the power line with a gripping mechanism. The gripping mechanism is designed for the weight and momentum of the aircraft to be sufficient enough to trip the mechanism for high-force perching. Once the gripper has been tripped, it grips the wire and the UAS rolls to hang and charge from the power line. After charging to completion, the active material actuator resets the gripper. The UAS then drops and resumes its mission.

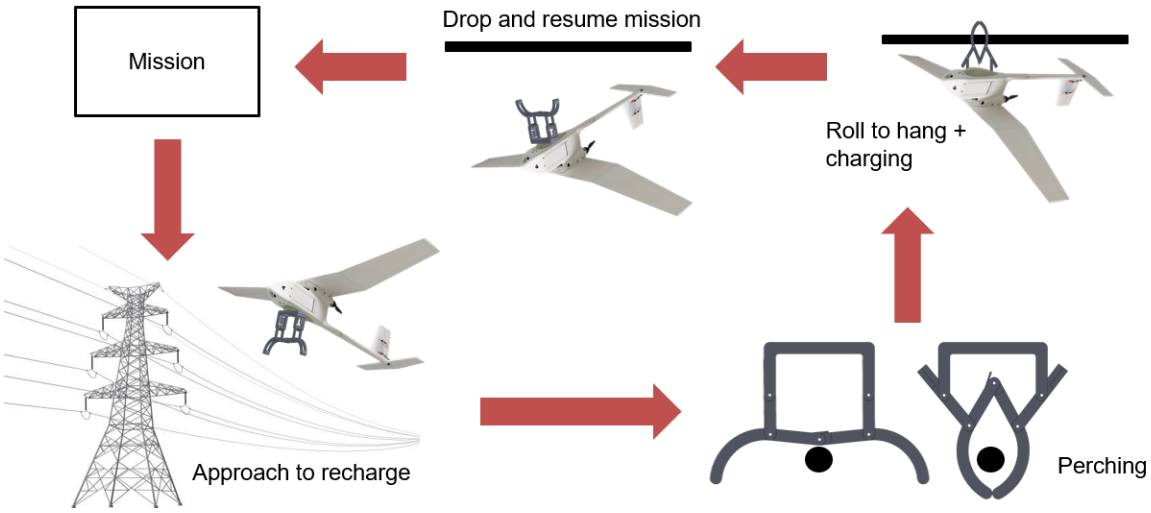

Figure 1.1: A graphical representation of the extended reconnaissance mission concept of operations.

1.3 Proposed Design Approach

This work proposes a bi-stable active material actuated gripping mechanism that recharges via surrounding infrastructure (e.g., power lines) by means of perching. The design operation cycle of the gripping mechanism is essential when considering integration of the mechanism with UAS. The perching mechanism is needed when the UAS batteries are nearly depleted and energy is most valuable. The perching mechanism must be passively actuated using only the pre-existing weight and moment of the aircraft. Therefore, the proposed bi-stable gripping mechanism will store strain energy while the UAS is perched and recharging, in preparation for bi-stable passive perching. Bi-stable passive perching paired with an active material reset mechanism enables efficient cyclical perching. In missions where energy is the most valuable resource for a UAS, the active material actuator will reset the gripping mechanism while it simultaneously stores elastic strain energy. The stored strain energy is produced by deforming the unique structure (e.g., deflecting a beam) of the mechanism. A mechanically bi-stable mechanism provides the UAS with the ability to perch without the need for additional electrical energy. This will allow the aircraft to passively trip the mechanism for high-force perching without the need for additional sensing equipment. Active

material actuators are chosen for the reset mechanism as they provide the highest energy-to-mass and energy-to-volume ratios. When combined with a bi-stable design, they pose the lowest risk of missed-gripping, with minimal sensing requirements, of all known options. The cycle depicting simultaneous energy storage and usage is depicted in Figure 1.2.

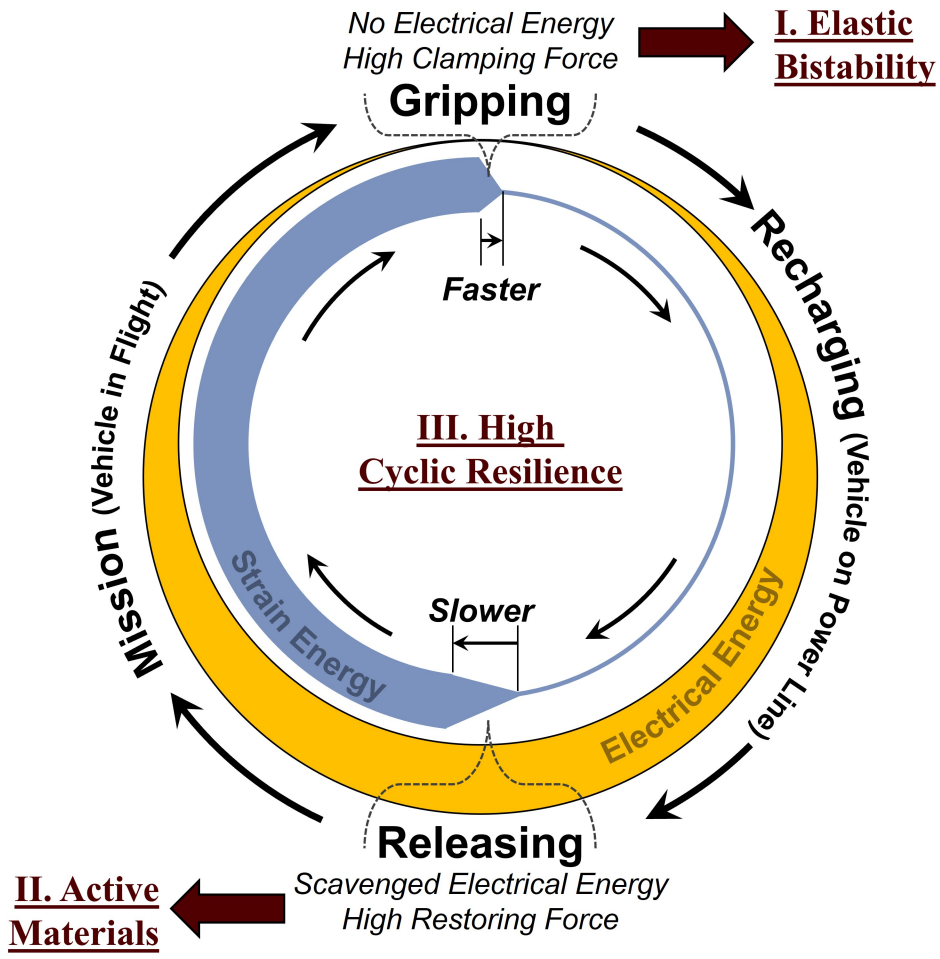

Figure 1.2: The cycle of stored strain energy produced by active material actuation and expended for efficient bi-stable high-force passive perching.

Design Problem

The RQ-11 RAVEN B UAS has been selected for gripper sizing and performance requirements. The UAS weighs 19.5 N with a wingspan of 1.4 meters. The RAVEN B has a cruise speed of 8.9

m/s and a cruise altitude of 76.2 meters above sea level [8]. All necessary parameters for the given problem can be calculated using these parameters and the following assumptions.

Flight profile and aircraft assumptions:

1. **Cruise speed**: It is assumed that the aircraft will be in steady level cruise for the majority of reconnaissance and intelligence missions. The cruise speed is assumed to be 8.9 m/s.

2. **Cruise altitude**: An aircraft cruise altitude is assumed in order to calculate free stream air density and dynamic pressure for drag calculations of the gripper mechanism. The cruise altitude is assumed to be 76.2 meters.

3. **Wing dihedral**: In order to estimate the area of the wing with simple geometry from a top view photo, the wings are assumed to be flat (no dihedral).

4. **Wet wing surface area (S_W)**: In an effort to simplify the calculations of drag without the need for panel methods or computational fluid dynamics, the aircraft wet wing area is conservatively assumed to be equal to that of the wing surface area.

5. **Oswald Efficiency Factor (e_0)**: The Oswald efficiency factor is assumed to be 0.85 for conventional fixed-wing aircraft with moderate aspect ratio and sweep.

The subsystem goals for development of a gripping mechanism for perching and recharging:

1. Maximize gripping force

   The gripping mechanism must have a gripping force that can carry the weight of the aircraft with margin for error. A factor of safety, S_F, of 1.2 is applied to the gripping force value of each design to ensure the mechanism can carry the weight of the aircraft. Thus, the lower constraint of gripping force, F_{grip}, is set to be exactly the weight of the aircraft. However, external factors (e.g., gusts, power line oscillation, etc.) may require a gripper that can carry more than just the weight of the aircraft. Therefore, the gripping force must be sufficiently large to ensure a wide range of potential external forces or environmental phenomena are

covered within the bounds of the design space. In an effort to reduce the size of the design space, the gripping force is assigned a high maximum constraint that is four times the weight of the aircraft. This ensures that computation time is not wasted on designs with unnecessarily high forces, while still exploring high-force designs. Therefore, the gripping force constraint is defined to be no less than the weight of the aircraft and no greater than four times the weight of the aircraft, after a safety factor has been applied.

$$W_{ac} < F_{grip}/F_S < 4W_{ac} \tag{1.1}$$

2. Minimize tripping force

   The tripping force requires minimum and maximum constraints to ensure that the gripper is operational while in service. In order to remain operational, we must avoid spontaneous tripping events and we must design a gripper that can be tripped by the moment of the aircraft. Both events depend on a tripping force that is sufficiently high or low, respectively. In order to trip a bi-stable mechanism an applied force large enough to set the mechanism into motion is necessary. Therefore, to ensure that the gripper will not trip spontaneously in flight, it is necessary to add a minimum constraint to design a gripper with sufficiently high tripping force that cannot be overcome by external factors (e.g., air resistance, gusts, etc.). Therefore, the minimum constraint of tripping force is assumed to be half the weight of the aircraft. In addition, the gripper design requires a maximum constraint for the tripping force to avoid wasting computational time on gripper designs that cannot passively perch/trip, In order to passively trip, the momentum of the aircraft must overcome the tripping force of the mechanism while landing on the power line. Thus, the maximum tripping force is assumed to be no greater than two times the weight of the aircraft. A minimum and maximum constraint of half the weight of the aircraft and double the weight of the aircraft are imposed on the

tripping force of the mechanism with a safety factor applied.

$$W_{ac}/2 < F_{trip}/F_S < 2W_{ac} \tag{1.2}$$

3. Minimize Gripper Drag

   In this work, the gripping mechanism is not only required to perch and reset but also must not hinder the performance of the aircraft. Another factor that is important to consider for aircraft efficiency is the induced drag and the profile drag due to the aircraft. Therefore, the following section will derive the additional drag on the system due to the gripping mechanism, as we prepare for design and optimization of an efficient cyclical gripping mechanism for small fixed wing UAS. The system in this work is defined as both the UAS and the gripping mechanism. The total drag of the system, D, is the sum of the profile drag of the system, D^P, and the induced drag of the system, D^I.

$$D = D^P + D^I \tag{1.3}$$

   In order to derive an equation that represents the total drag of the system, we must derive equations for the total drag of the aircraft, D_{ac}, and the total drag of the gripper, D_g, the total drag due to the gripper on the system, is defined as the sum of the profile drag of the gripper, D_g^P, and the induced drag on the aircraft due to the gripper, D_g^I.

$$D_g = D_g^P + D_g^I \tag{1.4}$$

   The profile drag of the gripper, D_g^P, is the product of the total coefficient of drag of the gripper, C_{D_g}, multiplied by the frontal area of the gripper, S_g, and the dynamic pressure of the free stream flow, q_∞, surrounding the gripper in cruise flight. The values of the gripper total coefficient of drag, C_{D_g}, are assumed and calculated in Section 4.3. For the current discussion we assume the values are known. Therefore, the profile drag of the gripper is

represented by the following equation,

$$D_g^P = C_{D_g} S_g q_\infty. \tag{1.5}$$

The induced drag on the aircraft due to the gripper, D_g^I, is derived from total drag of the aircraft using the assumptions defined for the flight profile and aircraft. The total drag of the aircraft, D_{ac}, is the sum of the profile drag of the aircraft, D_{ac}^P, and the induced drag on the aircraft due to the aircraft and the gripper, D^I. The total drag of the aircraft is also be defined as the product of the aircraft total coefficient of drag, $C_{D_{ac}}$, the frontal area of the aircraft, S_{ac}, and the dynamic pressure of the free stream flow, q_∞,

$$D_{ac} = C_{D_{ac}} S_{ac} q_\infty, \tag{1.6}$$

where the aircraft total coefficient of drag is the sum of the aircraft profile drag coefficient, c_d and the total induced drag coefficient of the aircraft, $C_{D,i}$, described by the following equation,

$$C_{D_{ac}} = c_d + C_{D,i}. \tag{1.7}$$

Hence, the total drag of the aircraft can be restated in the following form,

$$\begin{aligned} D_{ac} &= D_{ac}^P + D^I \\ \text{where, } D_{ac}^P &= c_d S_{ac} q_\infty \\ D^I &= C_{D,i} S_{ac} q_\infty \end{aligned}$$

The aircraft profile drag, D_{ac}^P, is a value that would remain constant for the same aircraft with any gripping mechanism design. Therefore, the profile drag coefficient of the aircraft is neglected as we solve for the total drag due to the gripper on the system, D_g. The induced drag of the system, D^I, is the sum of the induced drag due to the aircraft, D_{ac}^I, and the

induced drag due to the gripper on the aircraft, D_g^I. In order to derive the induced drag due to the gripper, we must first decompose the induced drag of the system in terms of the induced drag due to the aircraft and the gripper. The induced drag of the system is defined by the the total induced drag coefficient of the aircraft, which is the square of the coefficient of lift of the aircraft divided by pi the Oswald efficiency factor, e_0, and the aspect ratio of the wing, AR.

$$C_{D,i} = \frac{C_L^2}{\pi e_0 AR} \tag{1.8}$$

where the aspect ratio of the wing is equal to the square of the span, b, divided by the surface area of the wing, S_w.

$$AR = b^2/S_w \tag{1.9}$$

Recall, assumption 1 states that the aircraft is in cruise. For an aircraft in cruise, lift, L, is equal to total weight of the system, W. For a UAS with a gripper attached to the fuselage, the weight of the system is the sum of the weight of the aircraft, W_{ac}, and the weight of the gripper, W_g. Thus, the lift equation for the system becomes,

$$L = W = W_{ac} + W_g = C_L S_w q_\infty. \tag{1.10}$$

Once Equation1.10 is rearranged in terms of coefficient of lift, C_L, it is substituted into Equation1.8 to define the total coefficient of induced drag on the aircraft in terms of the weight of the aircraft and the gripper. The induced drag from Equation1.8 is then defined in terms of the weight of the aircraft and the gripper as follows,

$$C_{D,i} = \frac{(W_{ac} + W_g)^2}{S_w^2 q_\infty^2 \pi AR}. \tag{1.11}$$

Taking the total coefficient of induced drag on the aircraft from Equation1.11 and substituting it into the equation for induced drag of the system from Equation1.12, yields induced

drag in terms of weight of the aircraft and weight of the gripper.

$$D^I = \frac{(W_{ac} + W_g)^2}{S_w^2 q_\infty \pi AR} S_{ac} \tag{1.12}$$

After expanding the equation for induced drag of the system it is clear that the term with a quadratic dependence on the weight of the aircraft represents the induced drag of the aircraft, while the terms with a linear and quadratic dependence on the weight of the gripper represent the induced drag due to the gripper.

$$\begin{aligned} D^I &= \frac{S_{ac}}{q_\infty S_w^2 \pi AR} W_{ac}^2 + \frac{2 W_{ac} S_{ac}}{q_\infty S_w^2 \pi AR} W_g + \frac{S_{ac}}{q_\infty S_w^2 \pi AR} W_g^2 \\ \text{where, } D_{ac}^I &= \frac{S_{ac}}{q_\infty S_w^2 \pi AR} W_{ac}^2 \\ D_g^I &= \frac{2 W_{ac} S_{ac}}{q_\infty S_w^2 \pi AR} W_g + \frac{S_{ac}}{q_\infty S_w^2 \pi AR} W_g^2 \end{aligned}$$

By substituting the equation found for induced drag of the system 1.12 into Equation1.6, the total drag of the system (expressed in terms of the gripper mechanism parameters weight and frontal area) can be written in expended form as shown in Equation1.13.

$$D = c_d S_{ac} q_\infty + \frac{W_{ac}^2 S_{ac}}{q_\infty S_w^2 \pi AR} + \frac{2 W_{ac} S_{ac}}{q_\infty S_w^2 \pi AR} W_g + \frac{S_{ac}}{q_\infty S_w^2 \pi AR} W_g^2 + C_{D_g} S_g q_\infty \tag{1.13}$$

Recall, the aircraft profile drag coefficient is constant and therefore neglected while only considering the drag due the gripping mechanism. In order to do so, an equation for the reference total drag of the aircraft (without the gripper) is required.

$$D_{ac}^0 = (c_d S_{ac} + \frac{W_{ac}^2 S_{ac}}{q_\infty^2 S_w^2 \pi AR}) q_\infty \tag{1.14}$$

The reference total drag of the aircraft (Equation1.14) is subtracted from the total drag of the

system (Equation1.13) to yield the total drag of the gripper.

$$D_g = D - D_{ac}^0 = \frac{2W_{ac}S_{ac}}{q_\infty S_w^2 \pi AR} W_g + \frac{S_{ac}}{q_\infty S_w^2 \pi AR} W_g^2 + C_{D_g} S_g q_\infty \tag{1.15}$$

The total drag due to the gripper includes the induced drag on the aircraft due to the weight of the gripper and the profile drag of the gripper. As a result, we notice that the frontal area is linearly proportional to drag due to the gripper, D_g,

$$D_g \propto S_g \tag{1.16}$$

and the weight is quadratically proportional to the drag. Therefore, a gripping mechanism structure with lower weight leads to a quadratic decrease in drag as shown in Equation1.17.

$$D_g \propto C_{D,i} \propto (W_g)^2 \tag{1.17}$$

Hence, reducing the frontal area and weight of the mechanism would improve performance and efficiency of the overall system.

4. Reset via an active material

   An active material actuator is an active material that converts other forms of energy (e.g., electrical, chemical, thermal) into mechanical work. Common active material actuator configurations (e.g., wires, strips, tubes, etc.) are significantly more compact than the majority of servo motor pulley or servo motor belt driven gear systems. Therefore, an actuator must be designed to withstand the loads due to high-force gripping and recover enough strain to reset the mechanism to its reference state.

1.4 Breakdown of Contributions

Before moving forward, I would like to thank the gripper research team for all of their hard work. It was a pleasure leading such a bright team. Without the contributions of Peter Myers, Alex Lenhard, Kishore Yelchuri, and Bruhudithya Balaji, solving such an involved design problem would not have been possible. The major portions of this thesis that each of them contributed to are expressed in Table 1.1 for a more specific acknowledgement of their efforts.

Task	El-Ashkar Contribution	Acknowledgements
FEA Model Development	40%	Peter, Alex, and Kishore
FEA Scripting and post process	40%	Peter and Alex
DOE and optimization study	100%	
Experimental validation	100%	
Active material demo	50%	Bruhu

Table 1.1: Percent Contribution Table.

2. DESIGN CONCEPTS

In response to the needs of UAS for the extended reconnaissance mission discussed in chapter 1, the proposed conceptual gripper designs have the ability to enable UAS perching without additional power from the limited battery life of the UAS. The gripping mechanisms will take advantage of different techniques for storing strain energy to make passive perching possible. The following subsections will discuss the different mechanism designs that enable bi-stable high-force passive perching and the physical principals that govern each design concept. The mechanisms will be described in terms of their location in the perching cycle.

2.1 Bi-stable Bending Low Profile Design Concept

The bi-stable bending beam design draws inspiration from a mechanism known as a frog grabber or frog gaff [9, 10]. The design is intended to provide a low drag gripping option that is driven by stored strain energy in beams, mechanical bi-stability, and linear active material actuators to reset the mechanism.

Figure 2.1: Low Profile Gripper Design Concept.

The following discussion begins with the the gripper in the open state (reference state) of the perching cycle. In the open state, the jaw is open and strain energy is stored in preparation for perching, as shown in Figure 2.1. The low profile mechanism stores elastic strain energy in the deflected beams. Stored strain energy, U, in a deflected beam is directly proportional to the beam stiffness, K. The dimensions of the beam are varied to explore designs with optimal second

moments of area. The following equations relate the dimensions of the beam and beam deflection to the strain energy stored in the beam.

$$U = \int F du, \tag{2.1}$$

where

$$F = Ku. \tag{2.2}$$

From Euler Bernoulli Beam Theory, Equation 2.3 depicts the effects of length(L), width (w), and thickness (t) on the stiffness of the beam.

$$K = \frac{3EI}{L^3} \tag{2.3}$$

where,

$$I = \frac{wt^3}{12} \tag{2.4}$$

The following relations can be drawn from stiffness (Equation 2.3) and second moment of area (Equation 2.4) equations. The stored strain energy of the designed beam is directly proportional to the width of the beam, proportional to the cubed thickness, and inversely proportional to the cubed length.

$$U \propto K \propto w \propto t^3 \propto \frac{1}{L^3} \tag{2.5}$$

In the open state, the mechanism is ready for perching. A moment applied to the jaws deflect the beams until the jaw reaches the closed state, defined by a mechanical stop. The mechanical stop is what enables passive perching. The mechanism is bi-stable without the mechanical lock; however, the stable state without the mechanical stop would require far too much activation energy to excite the mechanism into the closed state.

2.2 Bi-stable Bending Strong Jaw Design Concept

The bi-stable strong jaw design concept also relies on stored elastic strain energy in deformed beams. However, the strong jaw concept is intended for structural efficiency rather than aerodynamic efficiency. Instead of prioritizing drag via low profile geometry designs, the strong jaw model will search the design space for efficient second moments of area enabled by the alternate hinge assembly.

Figure 2.2: Strong Jaw Gripper Design Concept.

The same engineering concepts and equations apply to the strong jaw design as shown in Equation 2.3 in the previous section. With these objectives, the strong jaw model should have higher forces for tripping the mechanism and gripping the power line.

Conceptually, the gripping force and tripping force outputted and required by the strong jaw design should be at least double that of the low profile model, neglecting effects due to the side-mounted hinges versus pin and barrel continuous hinges on the low profile model. This is because of the symmetry across the main front face of the gripper, adding an entire second set of jaws and a thicker beam connecting all four jaws.

2.3 Bi-stable Mechanism Design Concept

The bi-stable mechanism design concept, like the bi-stable bending low profile and strong jaw models, stores elastic strain energy in a deflected beam and is designed to reset via linear active material actuators. However, the mechanism exploits the bi-stability of a deflected beam fixed at both ends rather than mechanical instability. The initial state of the deflected beam fixed at both ends is defined as being in the open state (reference state), depicted in Figure 2.3. Using the bi-stable mechanism, the aircraft's weight and speed relative to the power line would need to produce a tripping force that can displace the beam past its neutral point in order to buckle into the closed state, shown on the right in Figure 2.3.

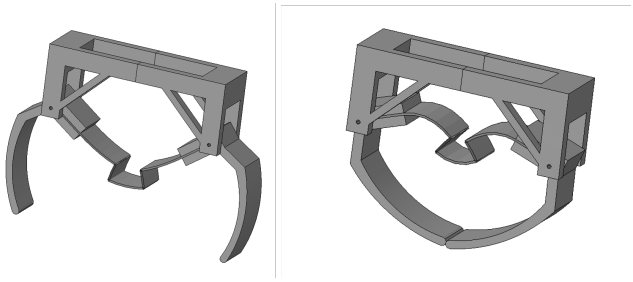

Figure 2.3: Bi-stable Mechanism Gripper Design Concept.

This bi-stable mechanism will also follow the general strain energy storage concepts discussed in regard to the beam stiffness equation from Equation 2.3. The complex geometry of the beam, shown in Figure 2.3, in this design will be the main difference. In this design, not only are thickness and length of the beam varied as design variables, but also the height and width of the compliant feature as described in Figure 2.4 and later in Section 3.3. Changes in the width (L_2) and height (L_3) will increase or decrease the second area of moment of the beam and directly affect beam stiffness according to Equation 2.3.

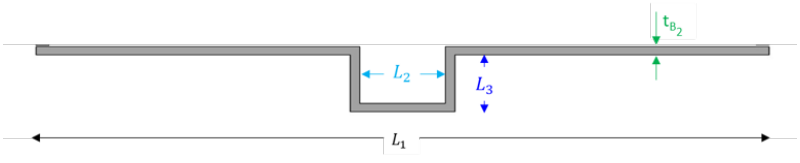

Figure 2.4: Bi-stable beam design variables.

2.4 Torsion Spring Design Concept

The torsion spring design is an alternative strain energy storage mechanism. The torsion spring mechanism is driven by stored elastic strain energy in torqued springs. The strain energy storage mechanism for this design concept depends on the stiffness of the spring rather than the stiffness of a beam. Hence, the strain energy of the spring due to deformation is given by,

$$U = \int \tau d\theta \tag{2.6}$$

where the torque of the spring is defined by the angular form of Hooke's law,

$$\tau = -K_s\theta \tag{2.7}$$

and the variation of strain energy stored is directly proportional to the spring stiffness coefficient, K_s, and torque angle, θ. When searching the design space, the spring stiffness coefficient will be varied while the torque angle is held constant.

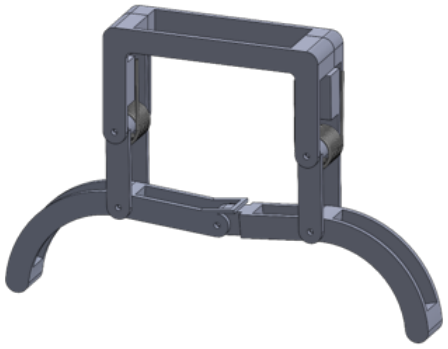

Figure 2.5: Torsion spring gripper design concept.

2.5 Active material actuators

Recall that extended reconnaissance missions will require robust and compact designs that eliminate the need to return to base. Therefore, all designs will rely on active material actuators, shown in Figure 2.6, to reset the mechanisms after charging to complete the perching cycle. The purpose of the active materials is to reset the mechanisms after they have been tripped. Each design concept would require a unique actuator design, but only the selected gripper design will be optimized for the final design.

The low profile design concepts is designed for a linear active material actuator. The top of the beam will serve as the base node to allow kinematic and positional control of the jaws. The linear actuator will connect the tip of the jaw to the end of the beam to produce a moment about the hinge. The moment must be large enough to deflect the beams and return the mechanism to the open state (depicted in the top left of Figure 2.6). The bi-stable strong jaw active material design will also follow that of the low profile design, favoring a linear active material actuator (depicted in the top right of Figure 2.6). The bi-stable mechanism will require a linear active material actuator designed to reset the mechanism. The active material will need to produce a large enough counter moment to overcome the buckled beam in the closed state (depicted in the bottom right of Figure 2.6). The torsion spring design concept will be designed for reset via an SMA torque tube that will counter the torque produced my the torsion spring (depicted in the bottom left of Figure 2.6).

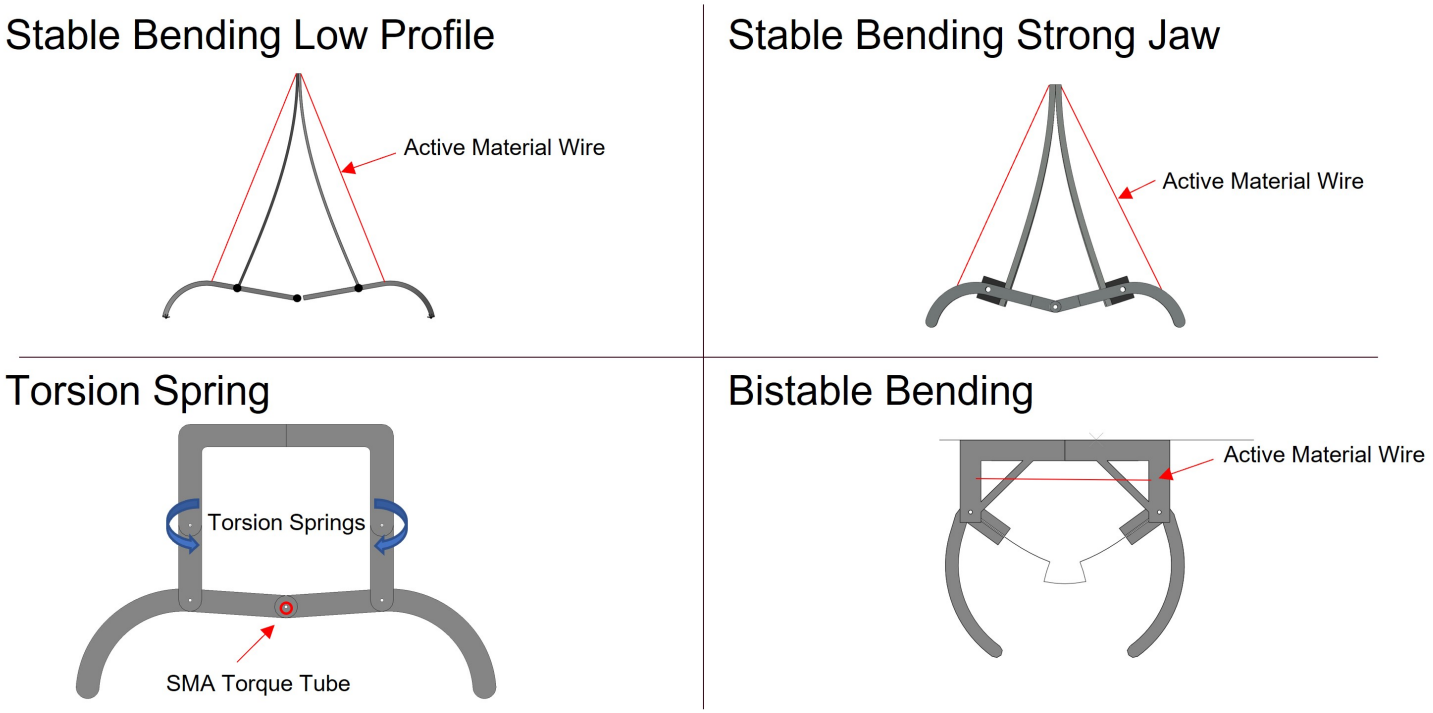

Figure 2.6: Conceptual gripper designs with active material actuators.

3. COMPUTATIONAL KINEMATIC AND DYNAMIC MODELING

All of the four bi-stable gripping mechanism design concepts will be dynamically analyzed with Abaqus FEA. Due to large rotations and displacements in a small amount of time, the Abaqus/Standard dynamic implicit solver is considered for this work. Bi-stable mechanisms that rely on large displacements and rotations for strain energy storage and high-speed perching (e.g., snap-through) require nonlinear geometry to simulate the dynamic response of the structure. This is because the effects of displacements and rotations on the stiffness matrix of the structure become too large to be neglected.

For general nonlinear dynamic analysis in Abaqus/Standard implicit, various time integration schemes are implemented to calculate the response of a system. The dynamic snap-through events associated with contact between the gripper and the power line require such an analysis over that of a general static analysis.

Abaqus/Standard implicit quasi-static time integration techniques will be implemented in this work. The advantage of using this quasi-static time integration technique is that it is unconditionally stable due to considerably high numerical energy dissipation. This allows for larger time steps when solving for dynamic quantities while still producing acceptable results and reducing run times. In addition, higher numerical energy dissipation allows for higher convergence rates without considering specific physical phenomena such as material dampening and frictional forces [11].

In the initial phase of kinematic and dynamic modeling, active materials are not included as they will not play a role in the down-selection process. The current study compares the required mission performance characteristics of the different strain storage and bi-stable mechanism designs.

3.1 Bi-stable Bending Low Profile Model

This section will describe the FE model of the low profile gripper mechanism design concept. The purpose of this dynamics simulation is to verify the kinematics and dynamics of the low profile gripper mechanism. This model will provide initial confirmation that the concept of storing strain energy in deformed beams will provide sufficient gripping forces that meet the mission constraints described in Section 1.3.

Finite Element Model Parts

The low profile design consists of a beam, jaw, and power line that are modeled as extruded shell elements and an analytical rigid surface, respectively. The beam length, width, and thickness three of many design variables that are listed and described in Chapter 4.1.

Finite Element Model Material Properties

As the intention for the prototypes is to validate the FE models, we consider our most reliable options for validation prototype fabrication. Therefore, a Markforged FX20 industrial 3D printer owned and operated by the US ARMY is selected. Onyx is a carbon-fiber composite with a silicon matrix designed and produced by Markforged. The properties of Onyx used for the FE models in this work are taken from the data sheets provided by Markforged [12] and listed in Table 3.1.

Property	Value
Tensile Modulus	2.4 GPa
Flexural Strength	71 MPa
Density	1200 kg/m^3

Table 3.1: Onyx Material Properties.

Finite Element Model Assembly

The bi-stable bending low profile model assembly contains two beams, two jaws, and three hinges. Each beam is attached to its corresponding jaw via pin and barrel continuous hinges. The two jaws are then attached to each other with a third hinge. Finally, the two beams are then assembled flush and bolted at the top. During the final step of assembly, the beams are initially deformed due to the the assembled jaw in between the two beams. In order to achieve the same initial deformation in the beams, the FE model requires that the assembly begin with the beam and jaw shells parallel as shown in Figure fig. 3.1. The jaws are then rotated away from each other about their respective hinges to achieve the initial deformation of the real assembly.

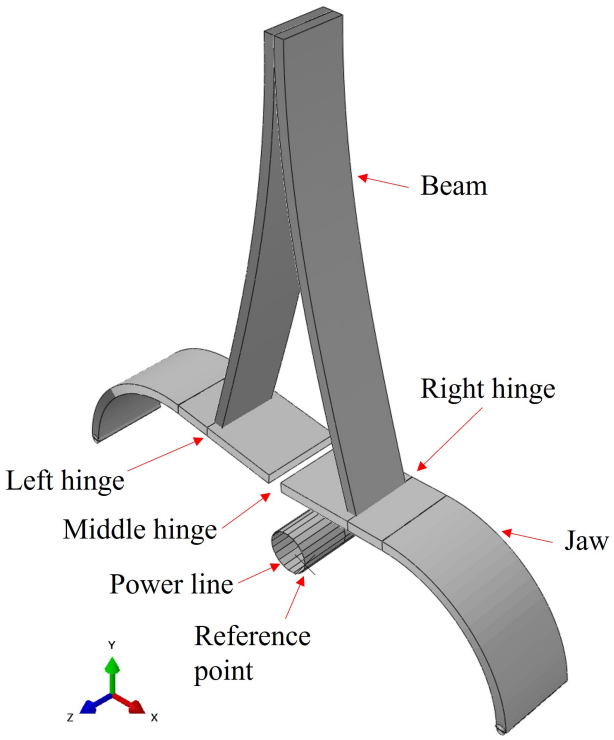

Figure 3.1: Low profile FEA assembly in the open state.

Finite Element Model Steps

The low profile model requires six dynamic steps with nonlinear geometry on to simulate the desired bi-stable behavior of the mechanism for perching and recharging.

1. Initial Assembly

   Step one depicts the model assembly before any boundary conditions have been applied. This state is only necessary for the FE models. In reality, the initial state is that of the closed state, as seen in steps 4, 5, and 6 of Figure 3.2.

2. Final Assembly

   In step two of Figure 3.2, the jaws are rotated about the z-axis to the assigned *stop angle* in preparation for the mechanism to trip. In other words, the mechanism is reset into the open state (reference state) as discussed in Section 2.1.

3. Open State Settling

   Open state settling allows the structure to dampen out to avoid disturbing the tripping step to follow.

4. Tripping

   To simulate tripping, the power line is displaced in the positive y-direction to push the middle hinge past its neutral point and trip the mechanism into a closed state.

5. Closed State Settling

   Step five is also a settling step to allow the structure to dampen out after high-force contact between the jaw tips.

6. Gripping

   To simulate gripping, the wire is pulled out of the closed jaws by applying a negative displacement in the y-direction to simulate the weight of the aircraft pulling the gripper off the power line.

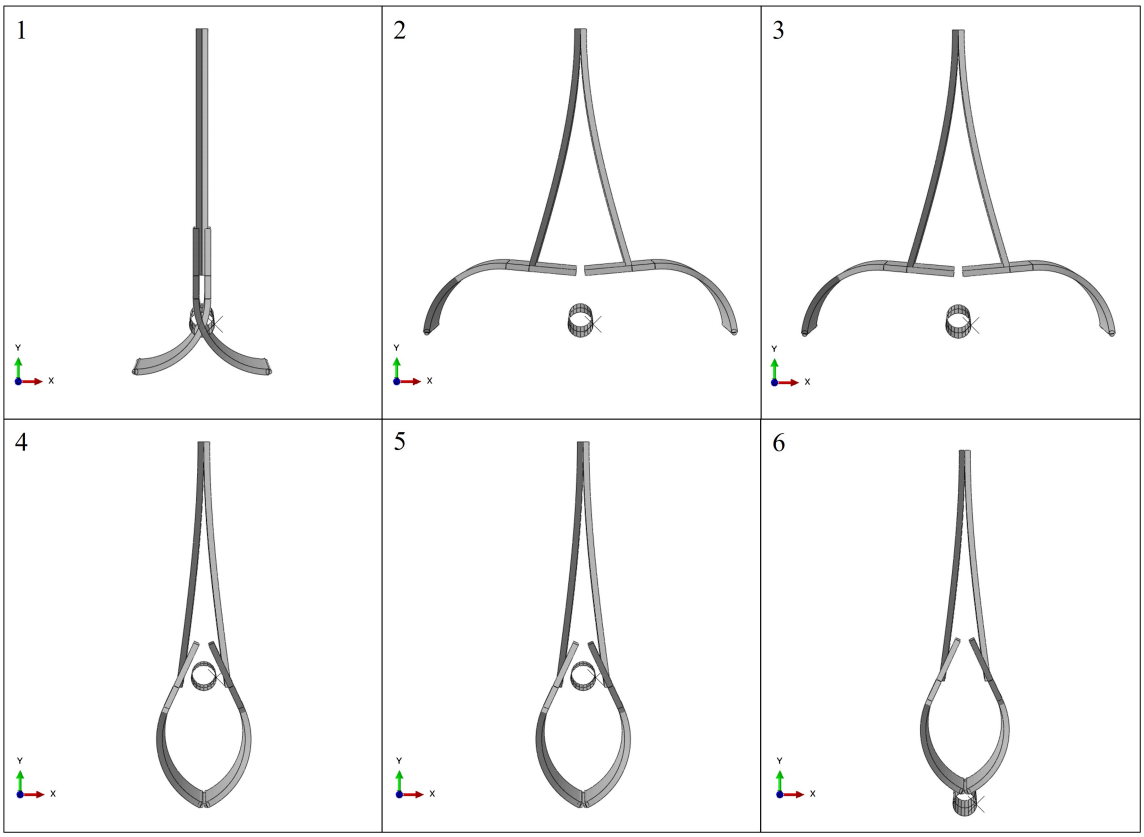

Figure 3.2: Low profile simulation steps.

Finite Element Model Interactions

Two types of interactions, contact and connector sections, were used to define the model for analysis. Frictionless hard contact was defined between the jaw tips as depicted in the left image of Figure 3.3. Frictionless contact was also defined between the power line and the power line-facing surface of the jaws.

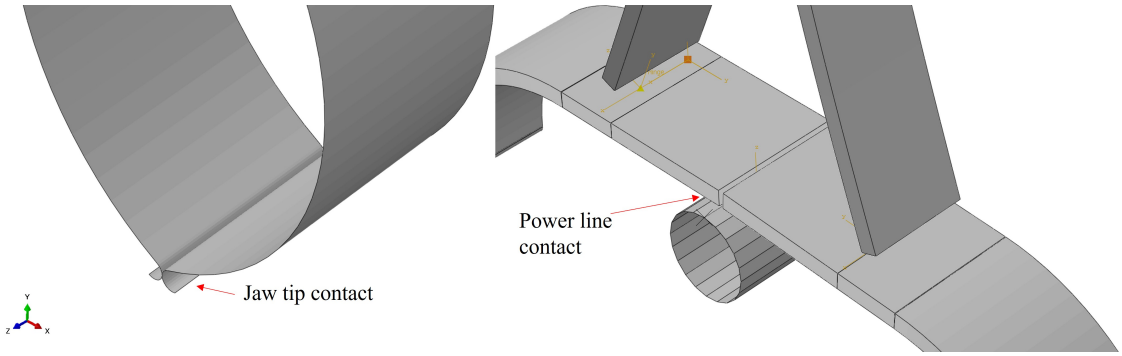

Figure 3.3: Low profile middle hinge connector.

Connector sections are defined between reference points (denoted as a triangle and square in Figure 3.4) to create a wire that behaves like a hinge. The wires define the center line about which the hinges will rotate and are positioned where the center of the hinges would be found in the a fabricated assembly.

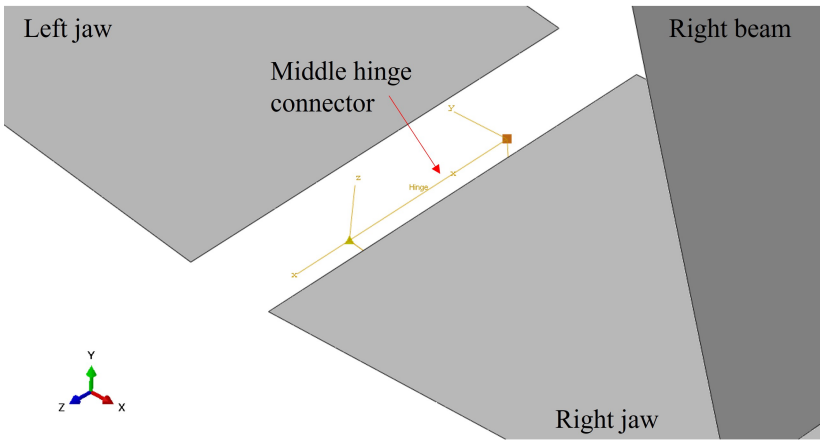

Figure 3.4: Low profile middle hinge connector.

Finite Element Model Loads and Boundary Conditions

Multiple boundary conditions were created for this analysis to simulate the dynamic motion of the bi-stable gripping mechanism. All steps include a boundary condition that fixes the top of the beams in space. This boundary condition does not allow the tip of the beams to displace or rotate in any direction. In order to open the gripper jaws and set the assembly into its final state (step 2 in Figure 3.2), equal and opposite rotation boundary conditions are created. The rotation boundary conditions are defined about the global z-direction and applied to each of the gripper jaws. The jaws are then rotated until they reach the assigned *stop angle* (described and depicted in Section 4.2.1 and Figure 4.2, respectively). The power line in the FE model is defined as an analytical rigid surface, defined by a reference point. A displacement boundary condition is applied to the power line in order to displace the power line for tripping and gripping simulation steps. The boundary condition holds the power line in place for assembly and settling steps and is modified to displace the power line in the y-direction to induce motion to the power line tripping and gripping steps.

Finite Element Model Parts Mesh

In the low profile FE model, a varying mesh was applied for efficient run times. In regions with contact forces as shown in Figure 3.3, the mesh seed size was decreased from 0.005 meters to 0.0005 meters along the length of the jaw. This adjustment was made to increase model convergence. The beam also has a seed size of 0.005 meters, just as the coarse parts of the jaw. S4R shell elements are used for both the beam and the jaw.

3.2 Bi-stable Bending Strong Jaw Model

This model is a subset of the bi-stable bending low profile model, both using stored strain energy in their main beams to enable gripping capability. The difference between them is that the strong jaw iteration features an alternate hinge assembly that is meant to enable designs with structurally efficient jaws. In other words, the jaw is split in two, to allow for jaw designs with more efficient second moments of area than seen in the low profile model.

Finite Element Model Parts

The strong jaw FE model is comprised of only primary parts and additional reference geometry. The primary parts are the main beam, the right hinge, the gripper jaw, and the power line. The main beam, the right hinge, and the gripper jaw are all continuum elements while the power line is made from an analytical rigid surface. The reference geometry consists of a contact plane (rigid analytical surface) in the YZ plane used to enable symmetry of the gripper by simulating contact between the gripper tips, shown in Figure 3.5.

Finite Element Mode Material Properties

As detailed earlier in this section, Onyx was our material of choice for this analysis. A section comprised of Onyx was created and applied to all solid geometry.

Finite Element Model Assembly

The strong jaw assembly consists of 5 part instances. The contact plane in the YZ plane was used as the central face about which the first symmetry boundary condition is applied. Moreover,

the contact plane acts in place of what would have been the reflected beam and jaw. The jaw was initially constrained and set into place vertically, but was rotated to get the outermost pin hole centered exactly with the YZ axis in order to accurately mimic the symmetry of the model when loads are applied in the analysis.

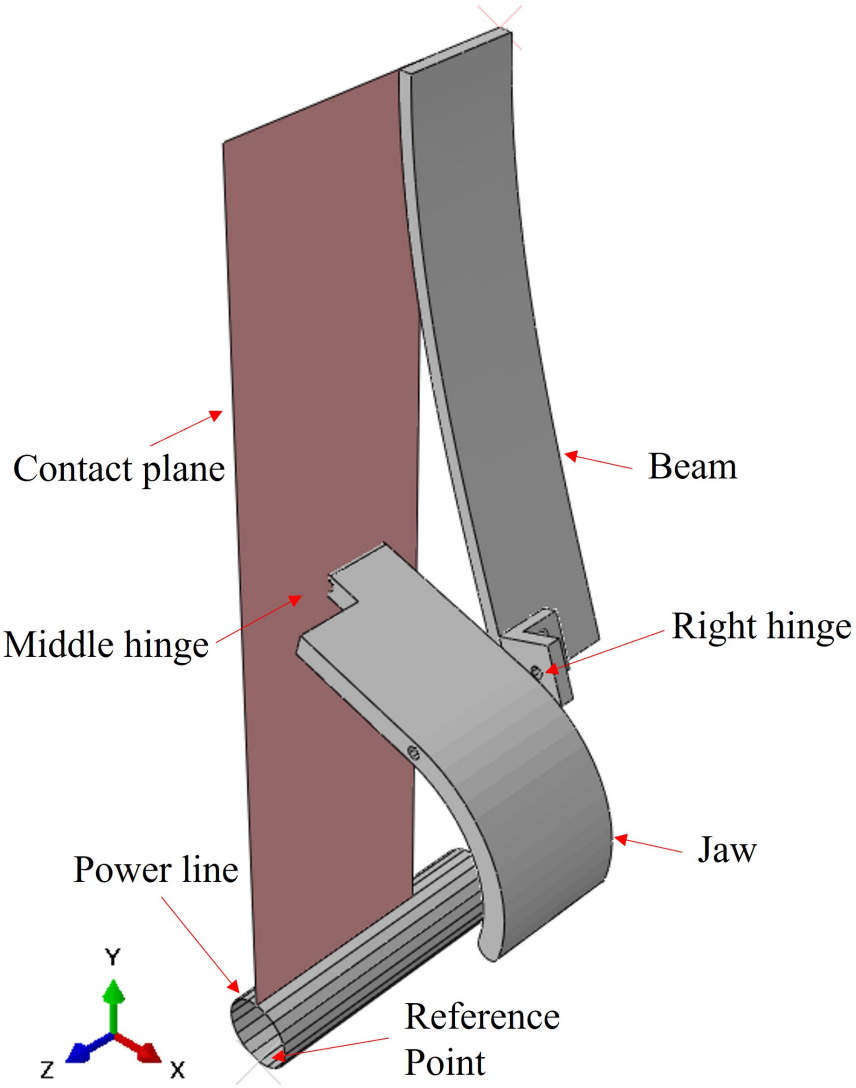

Figure 3.5: Strong Jaw FEA Assembly.

Finite Element Model Steps

The strong jaw model requires six dynamic steps with nonlinear geometry on to simulate the desired bi-stable behavior of the mechanism for perching and recharging.

1. Initial Assembly

   Step one depicts the model assembly before any boundary conditions have been applied. This state is only necessary for the FE models. In reality, the initial state is that of the closed state, as seen in steps 4, 5, and 6 of Figure 3.6.

2. Final Assembly

   In step two of Figure 3.6, the jaws are rotated about the z-axis to the assigned *stop angle* in preparation for the mechanism to trip. In other words, the mechanism is reset into the open state (reference state) as discussed in Section 2.2.

3. Open State Settling

   Open state settling allows the structure to dampen out to avoid disturbing the tripping step to follow.

4. Tripping

   To simulate tripping, the power line is displaced in the positive y-direction to push the middle hinge past its neutral point and trip the mechanism into a closed state.

5. Closed State Settling

   Closed state settling allows the structure to dampen out to avoid disturbing the gripping step to follow.

6. Gripping

   To simulate gripping, the wire is pulled out of the closed jaws by applying a negative displacement in the y-direction to simulate the weight of the aircraft pulling the gripper off the power line.

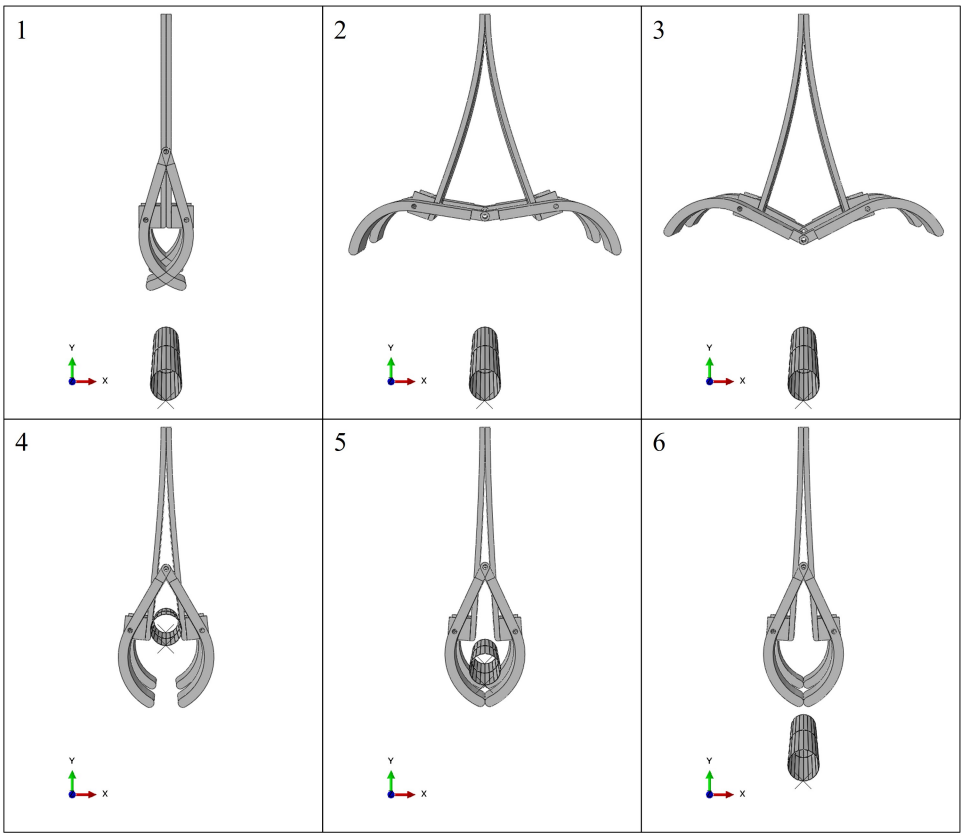

Figure 3.6: Strong Jaw Step Table.

Finite Element Model Interactions

Contact, constraints, and connector sections were all used to define the model for analysis and simulate real-life interactions. Contact and hinges are defined and built similar to the low profile model. The strong jaw model implements modified contact definitions to simulate the reflected half of the gripper that is excluded from the model. Frictionless hard contact was defined between the contact plane and the beam to simulate the presence of the symmetric beam. Similarly, frictionless contact is defined between the contact plane and the jaw tip to simulate the presence of the symmetric jaw. Both of these contact definitions are necessary to capture the interaction between the beam and jaw pairs. In Figure 3.5, the connector section that defines the hinge can be found along the center axis of the right hinge holes. The connector section wire, as depicted in Figure 3.4, is defined to be at the center of the concentric right hinge and jaw holes as shown in Figure 3.5.

Finite Element Model Loads and Boundary Conditions

Multiple boundary conditions were created for this analysis to simulate the dynamic motion that occurs in ideal operation of this concept. Three boundary conditions are applied to fix the contact plane in all directions, the gripper in the x and z-directions, and the top of the beam in all directions. Exactly as explained in the low profile model boundary conditions Section 3.1, a positive displacement is applied in the y-direction for the tripping and gripping step of the simulation. To reset the jaw for the final assembly step, a rotation boundary condition about the global z-direction is applied to the jaw to load the gripper to the open position as shown in Figure 3.6. The uniqueness of the strong jaw design is enabled by the two symmetry boundary conditions applied to the beam and jaw shown in Figure 3.5. A symmetry boundary condition is applied to capture the effects of the reflected beam and jaw pair about the YZ plane. A symmetry boundary condition is also need about the XY plane to simulate the remaining beam and jaw pairs. A depiction of the model with symmetry about the YZ and XY planes rendered can be found in Figure 3.5.

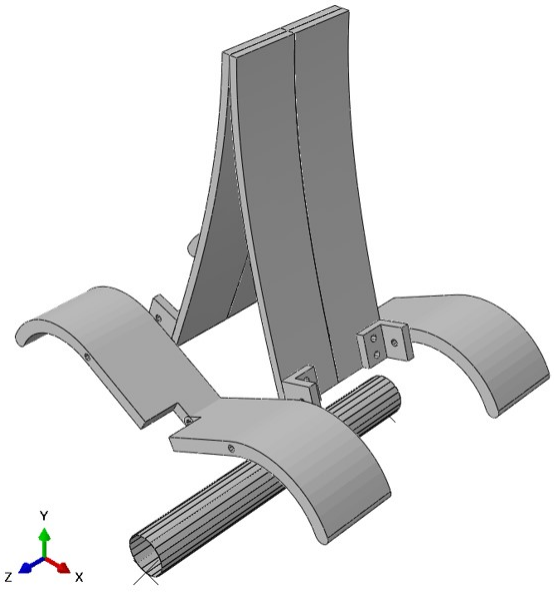

Figure 3.7: Strong Jaw with symmetry boundary conditions rendered.

Finite Element Model Parts Mesh

The three solid parts were meshed using the partitions defined earlier. A seed size of 0.01 meters was applied to seed the part and C3D8R elements were assigned to the mesh elements using the Mesh Element type option.

3.3 Bi-stable Mechanism Finite Element Model

Keeping true to the proposed design approach, the bi-stable mechanism works by having two stable states. This approach focuses on utilizing stiff 3D-printed composite beams for energy storage. The beam also acts as the trigger which transitions the mechanism between the open and closed states.

Finite Element Model Parts

There are four primary parts that make up the mechanism assembly with one secondary part that acts as reference geometry. The model consists of a gripper jaw and one half of the frame modeled as continuum element parts, a bi-stable beam (i.e, extruded shell) and a power line (i.e. analytical rigid shell), as well as a contact plane modeled as an analytically rigid surface. These components are assembled as seen in Figure 3.8.

Finite Element Model Material Properties

As detailed earlier in this section, Onyx was our material of choice for this analysis. A section comprised of Onyx was created and applied to all solid geometry.

Finite Element Model Assembly

The mechanism assembly is composed of two instances of both the gripper jaw and frame half and one instance of the bi-stable beam, power line, and contact plane, as depicted in Figure 3.8. The two frames are positioned opposite from each other with a required gap to deflect the bi-stable beam. The two jaws were positioned to line up the left and right hinge holes with their corresponding holes in the two frames. After which the bi-stable beam is positioned with either end placed in the jaw slots. Finally, to simulate the gripper fixed to the fuselage of the UAS, the

contact plane was positioned at the top surface of the frames in preparation for integration and boundary condition definitions.

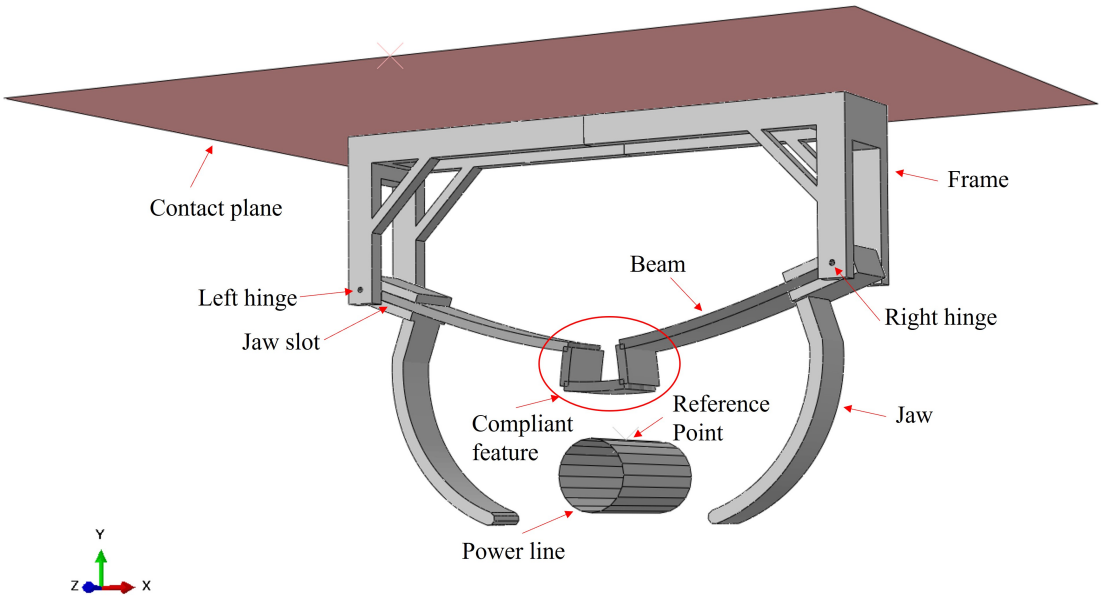

Figure 3.8: Bi-Stable FEA Assembly.

Finite Element Model Steps

The Bi-stable Mechanism model requires six dynamic steps with nonlinear geometry on to simulate the desired bi-stable behavior of the mechanism for perching and recharging.

1. Initial Assembly

   Step one depicts the model assembly before any boundary conditions have been applied. This state is only necessary for the FE models. In reality, the initial state is that of the closed state, as seen in steps 4, 5, and 6 of Figure 3.9.

2. Final Assembly

   In step two of Figure 3.9, the two halves of the frame are displaced equally and opposite in the x-direction and held in that position for the rest of the simulation in preparation for the mechanism to trip. In other words, the mechanism is reset into the open state (reference state) as discussed in Section 2.3.

3. Open State Settling

   Open state settling allows the structure to dampen out to avoid disturbing the tripping step to follow.

4. Tripping

   To simulate tripping, the power line is displaced in the positive y-direction to push the compliant feature past its neutral point and trip the mechanism into a closed state.

5. Closed State Settling

   Closed state settling allows the structure to dampen out to avoid disturbing the gripping step to follow.

6. Gripping

   To simulate gripping, the wire is pulled out of the closed jaws by applying a negative displacement in the y-direction to simulate the weight of the aircraft pulling the gripper off of the power line.

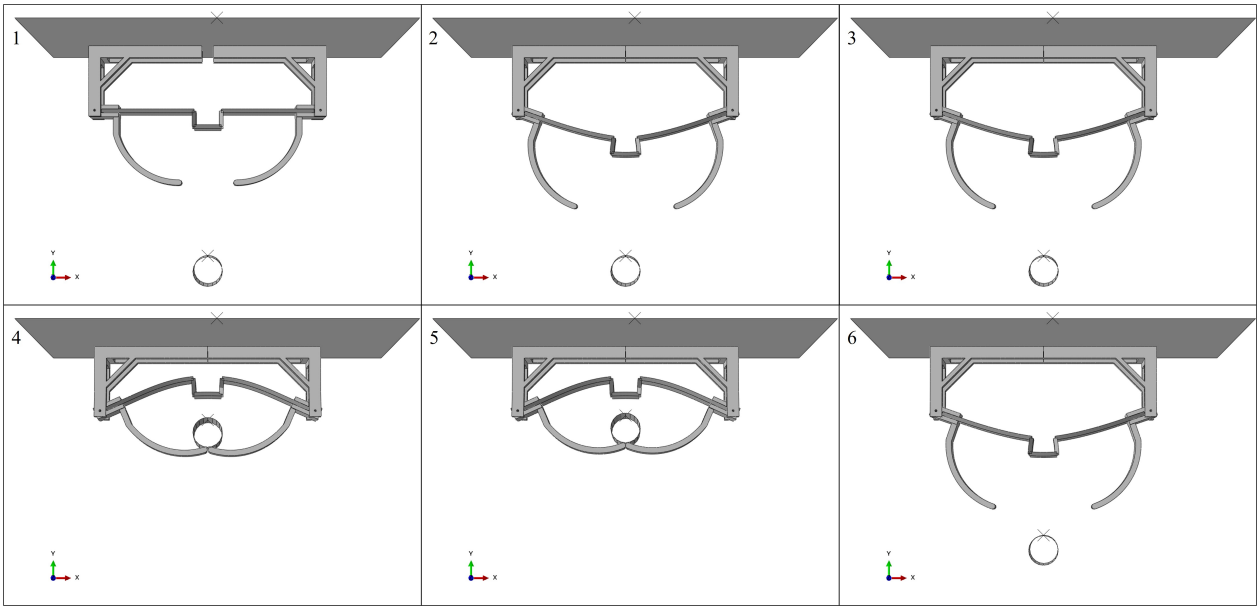

Figure 3.9: Bi-stable Mechanism Step Table.

Finite Element Model Interactions

The top and bottom surfaces of the bi-stable beam are tied with the top and bottom of the jaw slots. For the jaw to rotate freely about the frame, hinge connectors were built with respect to the jaw holes and frame holes using coupling constraints just as in the low profile model from Section 3.1. Frictionless contact is defined between the power line and the compliant feature, the power line and jaws, and between the jaw tips. Contact is also defined between the top surface of the frames and the contact plane; however, once the two surfaces have come in to contact, they can no longer be separated.

Finite Element Model Loads

The bi-stable mechanism only requires two types of displacement boundary condition to simulate gripping and tripping of the mechanism. Displacement boundary conditions were defined for the parts according to the step they are in during the simulation. The frames were displaced with an equal and opposite magnitude in the x-direction in order to deflect the beam. Without this displacement boundary condition, the beam would not be bi-stable and the mechanism would not function. Displacement boundary conditions are implemented to displace the power line in the y-direction for the tripping and gripping steps of the simulation.

Finite Element Model Parts Mesh

Partitions were used for the gripper jaws and frame to generate a structured mesh. A seed size of 0.01 meters was applied to seed the part and C3D8R elements were assigned to the mesh elements using the Mesh Element type option.

3.4 Torsion Spring Finite Element Model

The fourth gripper concept is distinct from the previous three because it uses aluminum torsion springs to store energy for the passive perching quick release mechanism. Similar to the strong jaw model, a symmetry boundary condition across the YZ plane is applied to reduce computation time. It shares a jaw shape with the other designs, but contains one extra joint along its arm than the other models. This allows the selected torsion spring to fit within the model.

Finite Element Model Parts

This design is comprised of six separate parts, three solid geometric parts and three 3D analytic rigid shells used to model the interactions and the spring. The geometric parts consist of the frame, the arm, and the jaw. The analytic shells consist of the power line, the contact plane in the YZ plane used for symmetry contact simulation, and a tube used to simulate the spring.

Finite Element Model Material Properties

As detailed earlier in this section, Onyx was our material of choice for this analysis. A section comprised of Onyx was created and applied to all solid geometry.

Finite Element Model Assembly

This design's assembly was built in a similar manner to all other assemblies. Only six position constraints were created to position the parts. The jaw was initially positioned horizontally but was rotated to its position in the open state. The center of the middle hinge hole on the jaw was position constrained in all directions but the *y*-direction, to simulate the reflected half of the model. The power line was also position constrained in all directions but the *y*-direction. Intended for the power line to impact the model directly in the center intersecting point between the two symmetric jaws for simplicity of analysis.

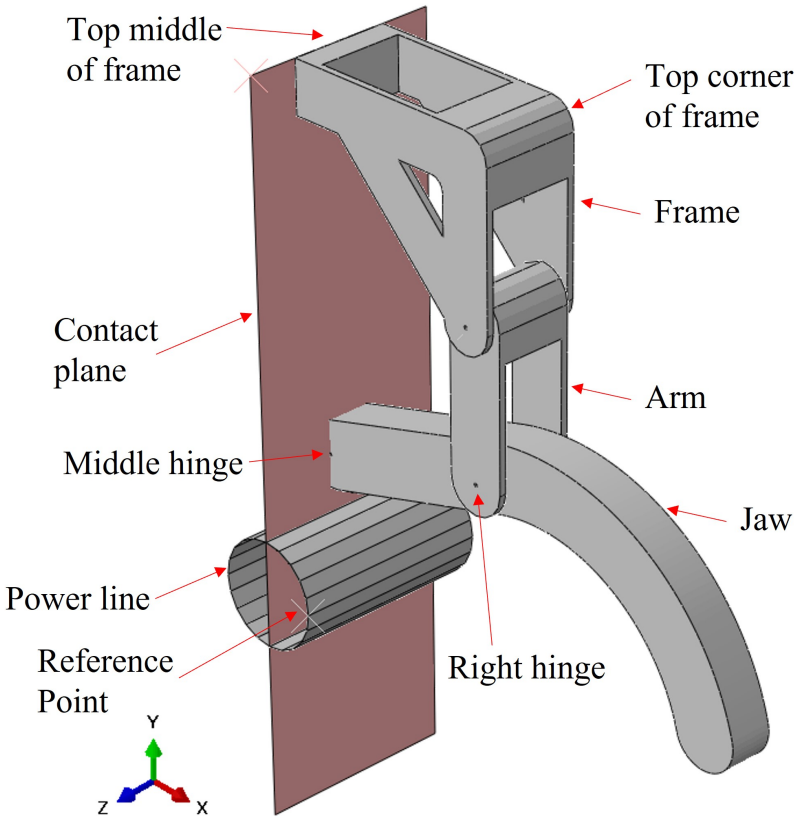

Figure 3.10: Torsion Spring FEA Assembly.

Finite Element Model Steps

The Bi-stable Mechanism model requires six dynamic steps with nonlinear geometry on to simulate the desired bi-stable behavior of the mechanism for perching and recharging.

1. Initial Assembly

   Step one depicts the model assembly before any boundary conditions have been applied. This state is only necessary for the FE models. In reality, the initial state is that of the closed state, as seen in steps 4, 5, and 6 of Figure 3.11.

2. Final Assembly

   In step two of Figure 3.11, the two analytical rigid shell cylinders that represent the torsion spring are torqued to load the quick release mechanism for passive perching. At the end of this step the gripper is in the open state and ready for perching, as discussed in Section 2.4.

3. Open State Settling

   Open state settling allows the structure to dampen out to avoid disturbing the tripping step to follow.

4. Tripping

   To simulate tripping, the power line is displaced in the positive y-direction to push the middle hinge past its neutral point and trip the mechanism into its closed state.

5. Closed State Settling

   Closed state settling allows the structure to dampen out to avoid disturbing the gripping step to follow.

6. Gripping

   To simulate gripping, the wire is pulled out of the closed jaws by applying a negative displacement in the y-direction to simulate the weight of the aircraft pulling the gripper off of the power line.

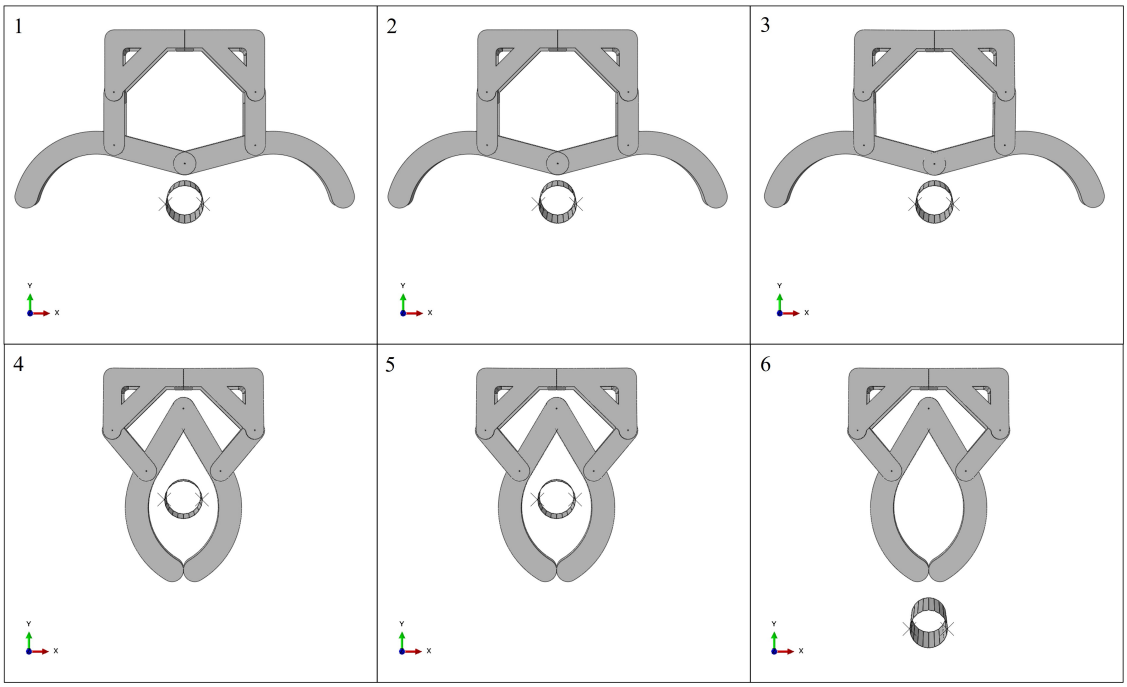

Figure 3.11: Torsion Spring Step Table.

Finite Element Model Interactions

Three types of interactions were used to define the analysis: contact, constraints, and a connector section. Two contact properties were defined, both for different purposes. Hard frictionless contact was used in three instances: between the power line and all inside surfaces of the jaw, the bottom of the frame and the inside of the jaw, and between the YZ contact plane and the inside tip of the jaw. The latter two contacts were created to simulate symmetry of the model. The second contact property was defined to have a rough friction formulation (i.e., includes friction) that was used between the analytical rigid shell representing the spring and the inside of the arm hole it was constrained to. In order to simulate the spring being locked after it had been torqued. Four coupling constraints were defined between reference points located in the center of the jaw and arm holes. Finally, a hinge connector section was defined within the right hinge hole to simulate a hinge similar to that of the low profile model, as shown in Figure 3.4.

Finite Element Model Loads

Multiple types of boundary conditions were created to simulate the dynamic behavior of the mechanism. A pin boundary condition is applied to keep the top middle of the frame from moving in any direction, while the top corner of the frame is allowed to displace in the x and y-directions. A displacement boundary condition is applied to the power line and modified with each step according to the function of the power line. During the tripping and gripping steps, the power line is displaced in the positive or negative y-direction to simulate tripping or gripping, respectively. A displacement boundary condition is also applied at the middle hinge hole to simulate a middle hinge. Since there is no actual hinge, the boundary condition constrains the motion of the middle hinge hole in the x and z-direction and only allows motion in the y-direction. To simulate the torsion spring, a rotation boundary condition is applied to the jaw about the global x-axis to load the spring. Finally, a symmetry boundary condition was applied about the YZ plane to simulate the reflected half of the torsion spring gripper. The complete torsion spring gripper mechanism is rendered in Figure 3.12.

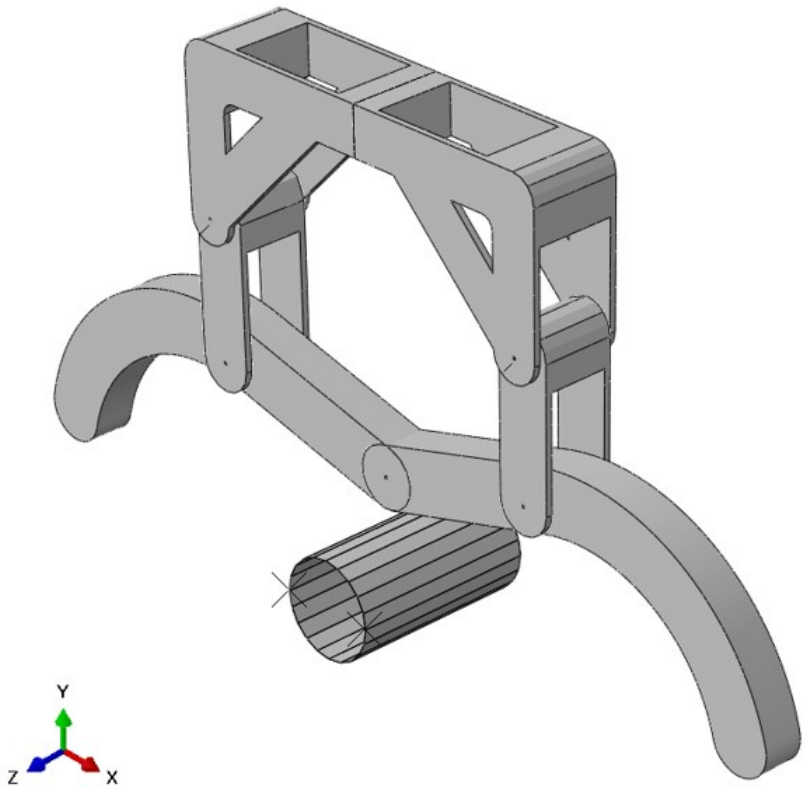

Figure 3.12: Torsion spring model rendered with symmetry.

Finite Element Model Parts Mesh

Like the two previous designs, the three solid parts were meshed using the partitions to generate a structured mesh. A seed size of 0.01 meters was applied to seed the part and C3D8R elements were assigned to the mesh elements using the Mesh Element type option.

3.5 Output Variables

All output variables are queried using a python post processing script that is agnostic to the designs. Thus, the same script is used for all models. In the case of tripping and gripping forces, the script is simply provided the node to query the reaction force from and the step during which it is to be queried. The mass is requested from Abaqus and is calculated based off of the material properties that have been defined in Section 3.1.

Tripping Force

The tripping force is queried from history output data that is saved with every time increment of the analysis. The tripping force is requested during the tripping step and is defined as the absolute value of the maximum force in the y-direction. Denoted in Figure 3.13 as the reaction force due to the force of the jaw on the wire, F_{JW}.

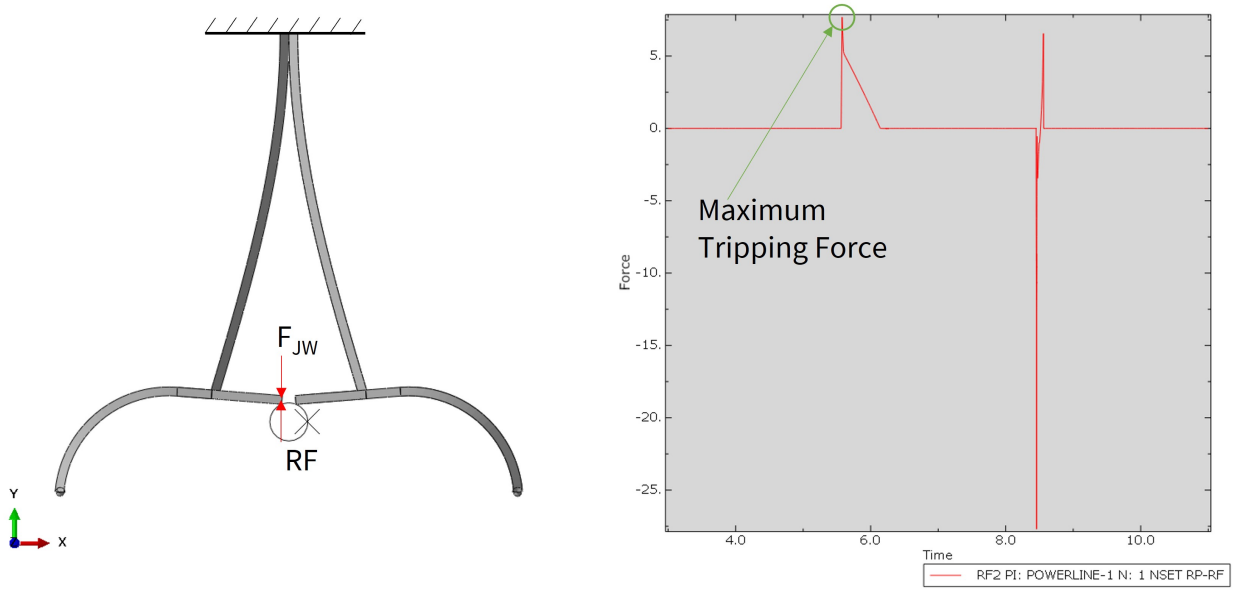

Figure 3.13: Tripping force schematic and time history.

Gripping Force

The gripping force is queried from history output data that is saved with every time increment of the analysis. The gripping force is requested during the gripping step and is defined as the absolute value of the maximum force in the y-direction. Denoted in Figure 3.14 as the reaction force due to the force of the jaw on the wire, F_{JW}.

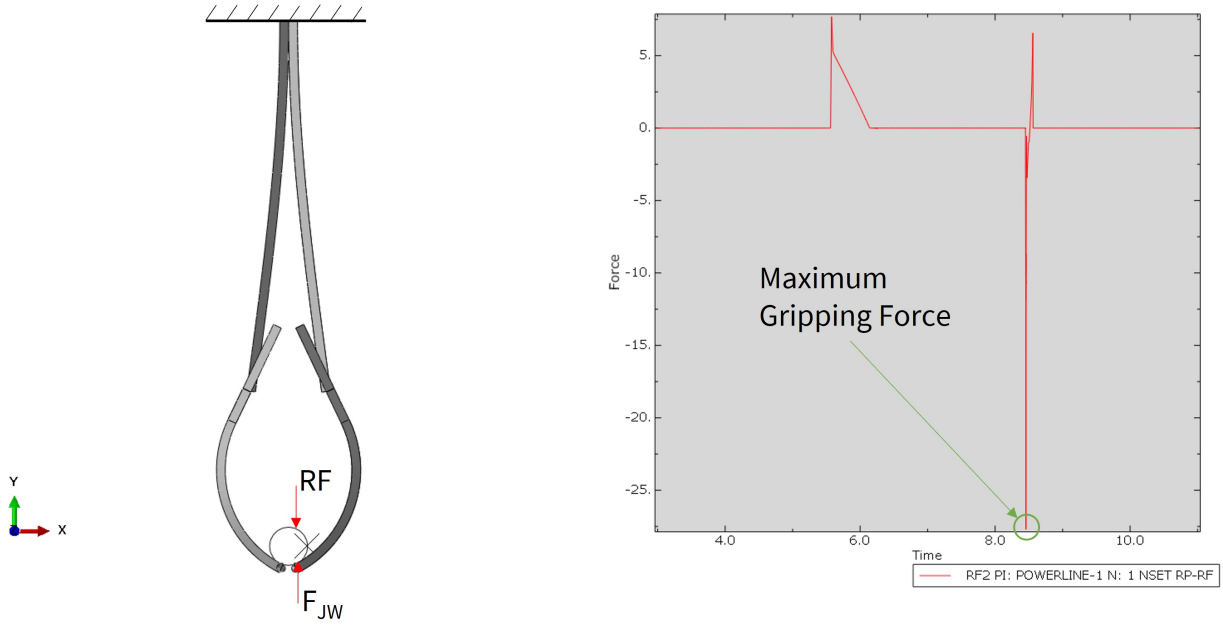

Figure 3.14: Gripping force schematic and time history.

Frontal Area

The importance and complication of the frontal area output variable requires its own validation section to elaborate more on the methods used to produce the value for each design. Each design's frontal area value is used to calculate the total induced drag on the aircraft due to the gripping mechanism. Therefore, it has direct relevance to the overall success of the mission scope.

Frontal area is calculated in a Python script that makes use of a pre-existing module called OpenCV. This script first takes an input of a black and white portable network graphic file with an image of the front-facing side of a gripper design, printed from Abaqus. Then, OpenCV is called to count the number of black pixels in the image, and pre-set model dimensions pulled from Abaqus are used calculate the approximate area of the gripper in square meters. This code was called during post-processing in order to parse through all saved Abaqus simulations and calculate the frontal area of each design. The script was validated against known shapes to ensure the validity of the script.

4. DESIGN OF EXPERIMENT

4.1 Design of Experiment and Pareto Optimality

This work will contain a design of experiment (DOE). In the DOE, the FE models will be parameterized and homogenized for design space exploration using a Latin hypercube sampling (LHS) technique. The design space will be defined using the parameters in Table 4.1, described later in Section 4.2. After the design space has been explored sufficiently, necessary adjustments can be made to the bounds that define the design space. As a result of homogenization, many designs share similar design variables or overlapping ranges. Similar design variables between the different models allows us to draw comparisons between the models. Sections 4.2.1, 4.2.2, 4.2.3, and 4.2.4 will describe the design variables in detail and provide context that describes the differences in the ranges and design variables corresponding to the behavior of each model.

LHS is a pseudo-random space-filling algorithm typically used when exploring a higher dimensional design space such as the one in this work. The selection of LHS as the algorithm for the DOE avoids the curse of dimensionality. For such a high dimensional problem with seven design variables, the number of runs for a Full Factorial DOE would have required 2187 runs (3^7 runs). The purpose of the DOE is to down-select and implement a computationally efficient design optimization in an effort to avoid such expensive brute force methods. Thus, a 100 sample LHS DOE will be performed for each model. The optimization scheme will be discussed further in chapter 6.

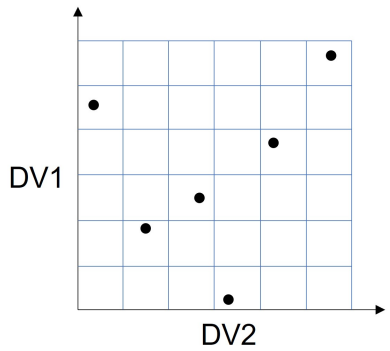

Figure 4.1: Example of Latin Hypercube Sampling.

4.2 Homogenization and Paramaterization

To make the DOE and the optimization possible, the FE models are scripted and parameterized. When building an Abaqus model in the user interface, each button clicked and number typed has a corresponding line of code that is printed in a "replay" file. For every model, the python code that corresponds to the buttons pressed and dimensions entered is copied and converted in a script. The script is then edited and the design variable dimensions are parameterized. This mean that the design variable and all its dependent dimensions and coordinates for part creation and assembly are represented in terms of the design variable. All the math and trigonometry becomes part of the Abaqus python script. This is necessary because the design variable is not variable via the code. Once the bounds of the DOE or optimization are set, the algorithm may then select different values permitted by the bounds and re-build the design as many times as requested. The following sections will describe the aforementioned design variables and why they were parameterized for each of the gripper design concepts.

Design Variable	LP	SJ	BM	TS
Jaw width factor	1 - 1.5	0.5 - 1.2	0.6 - 1	0.5 - 0.9
Jaw thickness	4 - 6 mm	7 - 13 mm	4 - 8 mm	15 - 20 mm
Width	2 - 4 cm	2(2 - 5) cm	2 - 4 cm	2 - 4 cm
Beam thickness	4 - 8 mm	4 - 8 mm	2 - 5 mm	-
Stop Angle	5° - 10°	0° - 10°	-	6.5° - 20°
Beam-jaw length	4 - 6 cm	5 - 7 cm	-	5 - 8 cm
Beam length	15 - 25 cm	15 - 20 cm	-	-
Compliant feature height factor	-	-	0.1 - 0.25	-
Compliant feature width factor	-	-	0.05 - 0.15	-
Frame length	-	-	17 - 21 cm	-
Arm thickness	-	-	-	1.5 - 2 cm
Spring stiffness	-	-	-	0.025 - 0.5 Nm/rad

Table 4.1: Design of Experiment Bounds.

4.2.1 Low Profile Model Paramaterization

The low profile model design is parameterized using seven design variables. The design variables are listed below and their effects on the performance of the model and or each other will be explained in this section.

1. Beam length

   The beam length is an important parameter of this design due to the effect that length has on beam stiffness. From Equations 2.3 and 2.4 in earlier sections we can see that,

   $$K \propto 1/L^3, \tag{4.1}$$

   the stiffness of the beam is inversely proportional to the length of the beam cubed. Thus, the length of the beam would largely impact gripping and tripping force.

2. Beam thickness

   The beam thickness has a similar effect on the performance of the mechanism in the fact that it directly affects stiffness of the beam as well. The effects of thickness on stiffness can be seen in Equations 2.3 and 2.4. Where the thickness, b, is proportional to the stiffness of the beam as such,

   $$K \propto b. \tag{4.2}$$

   The stiffness of the beam is proportional to the thickness of the beam, which comes directly from the moment of inertia of a cantilevered beam (equation 2.4).

3. Beam width

   The beam width also follows suit and the effect it has on the performance of the beam can be explained using Equations 2.3 and 2.4. The width largely affects the stiffness of the beam and in turn the performance of the mechanism. The relationship between stiffness and width is as follows,

   $$K \propto h^3, \tag{4.3}$$

   where the stiffness is directly proportional to the width of the beam cubed.

4. Jaw thickness

   The jaw thickness parameter serves the purpose of decreasing the weight and frontal area of

the gripping mechanism. The effect of weight and frontal area on the aerodynamic performance of the gripping mechanism is quantified by drag shown in Section 1.3.

5. Jaw width factor

   The jaw width factor is an added parameter than helps decrease weight of the aircraft. The goal of varying this parameter is to ensure that the jaw can be as light as possible while remaining strong enough to withstand the stresses associated with high speed tripping and gripping.

6. Beam-jaw attachment point

   The beam-jaw attachment point is the length between the middle hinge and the hinge that attaches the beam to the jaw. This member can be seen as a moment arm that is varied to control tripping force.

7. Stop angle

   Similar to the function of the beam-jaw attachment point, the ability to vary stop angle is one more parameter that can affect tripping force. Both of these parameters change the maximum deflection of the beam and distance required to displace the middle hinge past its neutral point.

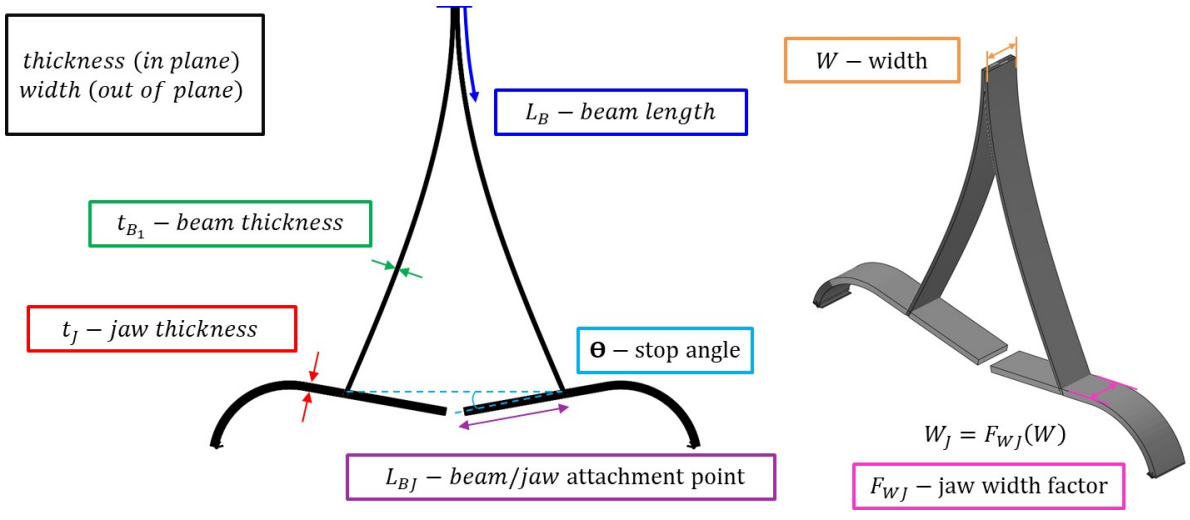

Figure 4.2: Low profile model design variables.

4.2.2 Strong Jaw Model Paramaterization

As in the low profile model, the strong jaw has seven design variables chosen to highlight the strengths of this specific design and drive the design space study to the optimal result for the intended mission set. The only difference between the design variables is that SJ beam width is the is the sum of both beam widths. This is due to the fact the SJ design concept includes two jaw and beam sets, as explained in Chapters 2 and 3 previously.

1. Beam length
2. Beam thickness
3. Beam width
4. Jaw thickness
5. Jaw width factor
6. Beam-jaw attachment point
7. Stop angle

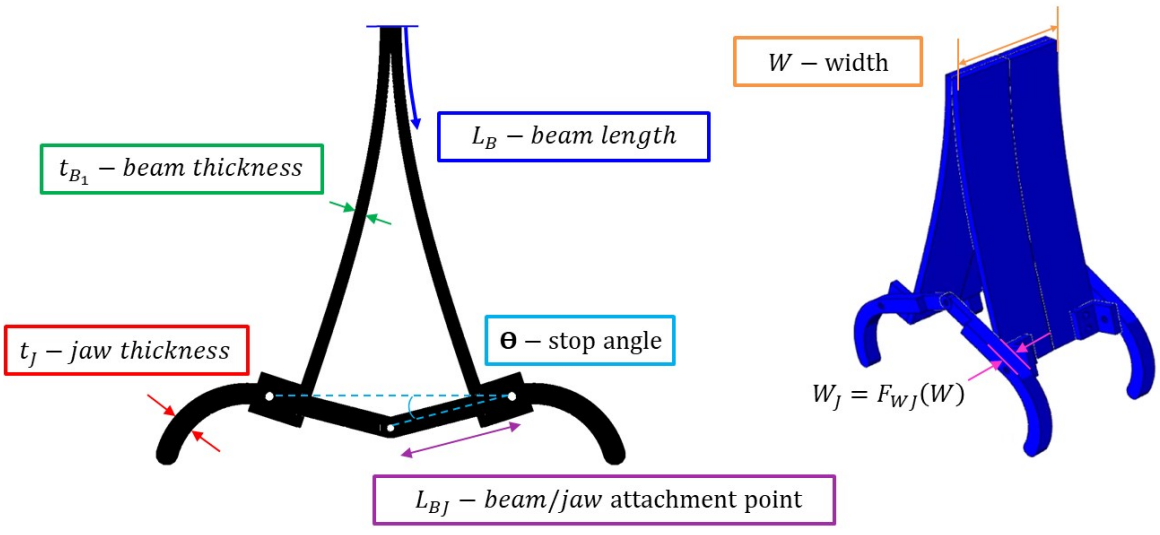

Figure 4.3: Strong jaw model design variables.

4.2.3 Bi-stable Mechanism Model Paramaterization

The bi-stable mechanism model design in parameterized using seven design variables. The design variables are listed below and their effects on the performance of the model and or each other will be explained in this section.

1. Frame length

   The frame is a critical design variable for two reasons. First, the difference in length between the undeformed bi-stable beam and the frame length, depicted in Figure 4.4 as ΔL_{41}, sets the strain energy storage capacity of the mechanism. The greater the deformation strain the bi-stable beam undergoes, the greater the strain energy stored by the mechanism. Second, the frame of the BM model must be rigid due to the torsional loads imposed by buckling of the bi-stable beam. Introducing another trade off between stiffness, weight, and energy stored due to deformation strain.

2. Frame width

   The width of the frame is a driving dimension from which width of the bi-stable beam and width of the jaw are derived. These widths play an important role in the overall weight of the mechanism and are minimized until maximum von Mises stress constraint are violated.

3. Beam thickness

   Although the bi-stable beam in this model is a complex beam. The same principles apply as discussed in the previous two sections. Stiffness of the beam is proportional to the thickness of the beam.

4. Compliant feature height factor

   The height of the beam compliant feature is also directly proportional to the stiffness of the beam. This parameter offers the optimizer one more parameter to indirectly explore buckling phenomena of the complex beam in order control the magnitude of tripping and gripping force.

5. Compliant feature width factor

   Same as for the thickness of the beam and the height of the beam compliant feature, the width of the beam compliant feature is also directly proportional to the stiffness of the beam. This parameter offers the optimizer a third parameter to indirectly explore buckling phenomena of the complex beam in order control the magnitude of tripping and gripping force.

6. Jaw thickness

   The jaw thickness parameter provides the optimizer with additional control over the weight of the mechanism. The dimension is minimized as long as the maximum von Mises stress constraint is not violated.

7. Jaw width factor

   The jaw width factor is another parameter that provides the optimizer control over the mass of the mechanism while simultaneously trading off the mass for an increase in stress.

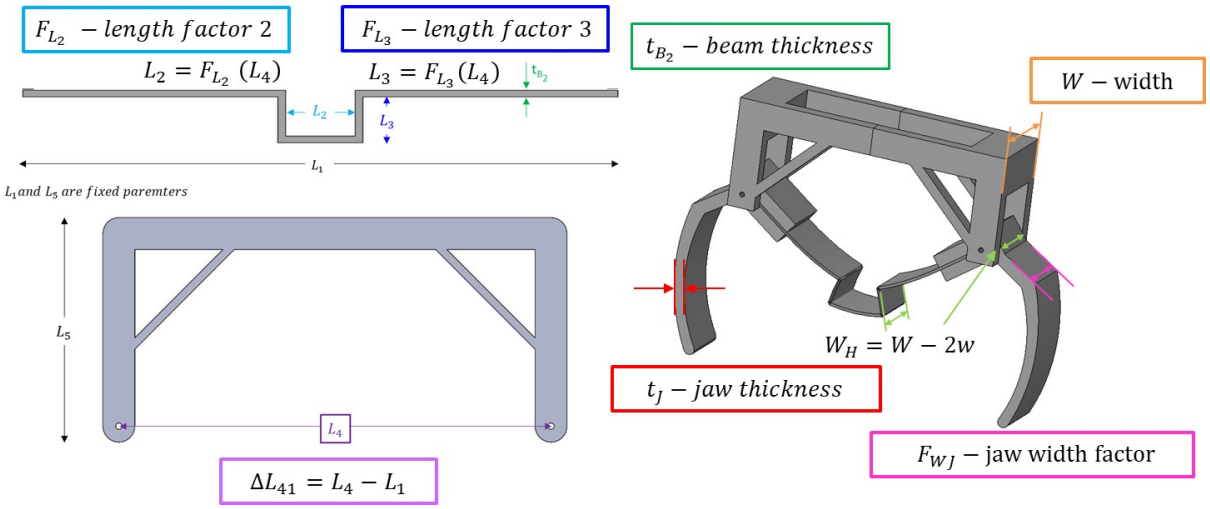

Figure 4.4: Bi-stable mechanism model design variables.

4.2.4 Torsion Spring Paramaterization

The torsion spring design variables are unique to the design but still have design variables in common with the previous three designs.

1. Frame width

   Similar to the frame width defined for the BM model, the width is a driving dimension from which width of the arm and width of the jaw are derived. These widths play an important role in the overall weight of the mechanism and are minimized until the maximum von Mises stress constraint is violated.

2. Arm thickness

   Arm thickness is a design variable that must be minimized without violating maximum von Mises stress criterion. This design variable was also created in an effort to allow the optimizer to minimize mass, surface area, and in turn drag of the gripping mechanism.

3. Spring constant

   Unlike the previous three designs, the strain energy stored in the TS model is due to deformation of a torque spring instead of a beam. The spring stiffness coefficient determines the stiffness of the spring as described by Equation 2.7 from previous discussions.

4. Beam-jaw attachment point

   The beam-jaw attachment point is the length between the middle hinge and the hinge that attaches the arm to the jaw. This member can be seen as a moment arm that is varied to control tripping force. The longer the moment arm, the lower tripping force becomes.

5. Stop angle

   Similar to the function of the beam-jaw attachment point, the ability to vary stop angle is one more parameter that can affect tripping force. Both of these parameters change the distance required to displace the middle hinge past its neutral point to initiate tripping.

6. Jaw thickness

   The jaw thickness parameter provides the optimizer with additional control over the weight of the mechanism. The dimension is minimized as long as the maximum von Mises stress constraint is not violated.

7. Jaw width factor

   The jaw width factor is another parameter provides the optimizer control over the mass of the mechanism while simultaneously trading off the mass for an increase in stress.

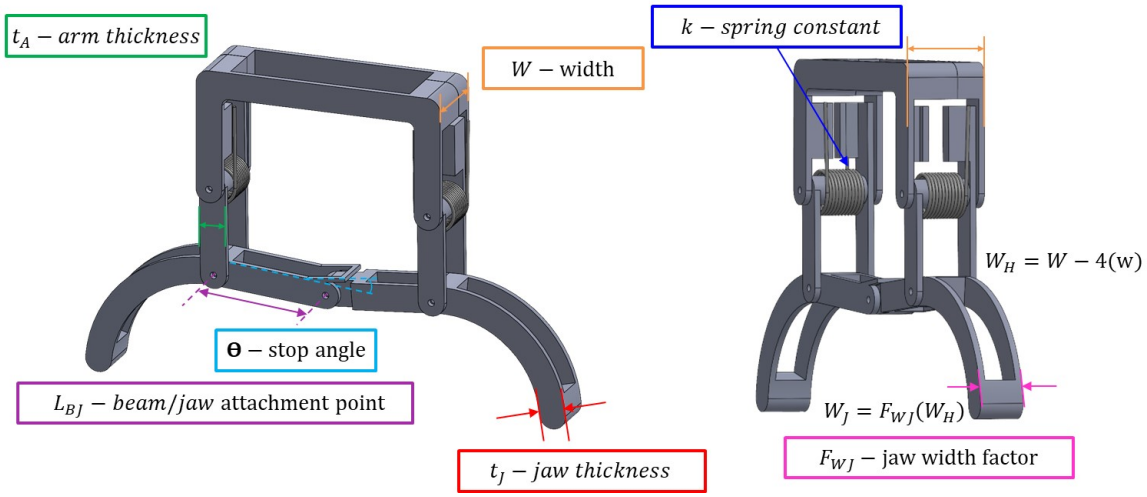

Figure 4.5: Strong jaw model design variables.

Testing the designs with high forces and large motion would provide more accurate test data. Therefore, a preliminary LHS DOE is performed before validation. To ensure that the models will not fail during testing, this data is subjected to a higher safety factor applied to the maximum von Mises stress, tripping force, and gripping force. The designs with the largest forces are selected from the preliminary DOE and are prototyped for validation testing discussed in Chapter 5. A safety factor of 1.667 is chosen to be conservative in an effort to keep the models from breaking during testing.

The data from the final DOE will be subjected to low safety factors in an effort to reduce weight and in turn drag. The gripping mechanisms are compared with respect to the output variables that best suit the missions requirements. In this work the most important mission requirement is that the gripping force should be large enough to carry the weight of the aircraft. Second, the tripping force is not too low as to induce tripping while in flight and not too high as to keep the mechanism from tripping when landing on a power line or similar structure. Third, the gripper drag must be minimized to avoid impeding the performance of the aircraft itself. Otherwise, the addition of the gripping mechanism would not enhance the performance of the UAS or benefit the extended reconnaissance mission, as discussed in Section 1.3.

4.2.5 Design Trade study

As this work heads towards down-selection, discussed in Section 4.3, it is important to examine the trade off between the output variables of the design problem. This is a necessary step to determine which of the designs would best fit the performance requirements of the mission. Therefore, this section will discuss 3D non-dominated frontiers corresponding to the non-dominated solutions of each model's LHS DOE in the design space.

To begin the analysis and comparison of all four gripping mechanisms, the Pareto optimality of the design is examined with respect to the non-dominated frontier of the unconstrained LHS DOE results. The initial comparison will be based purely off of the performance of the mechanism designs. In order to tie the comparison back to the drag of each gripping mechanism, the non-dominated frontiers for frontal area of the gripping mechanism as well as the mass of the gripping mechanism will be compared. The unconstrained 3D non-dominated frontiers are included for a raw data comparison from the results of the virtual experiments. Recall, the constraints applied to the problem will be as follows,

$$W_{ac} < F_{grip}/F_S < 4W_{ac}$$

$$W_{ac}/2 < F_{trip}/F_S < 2W_{ac}$$

$$\sigma F_S < \sigma_{yield}$$

The constraints will not change and are held constant for DOE and optimization. It is important to stress the constraints, because the Pareto frontier is defined with respect to the theoretical optimal solution, known as the utopia point. The 3D non-dominated frontiers in the plots are a subset of what is defined to be the Pareto frontier. Our non-dominated frontier is only as accurate as the sample size and quality. In this work, the LHS gives is a pseudo-random and semi-structured sample size; however, this does not ensure that the randomly selected design, although spread out semi-evenly, are the optimal solutions in the design space.

4.2.5.1 Gripping and Tripping Force vs. Frontal Area

The following Figures 4.6 and 4.7 depict a surface corresponding to the non-dominated frontier of designs in the objective space with respect to gripping force, tripping force, and frontal area. The frontal area in these plots corresponds to the unweighted profile drag of the gripping mechanism.

The profile drag plots will give us an idea of how the non-dominated frontiers compare for each design with respect to gripping and tripping force as a result of varying the geometry. Varying the geometry of the parameterized models affects the aerodynamics of the mechanisms in addition to the structural response. It is important to note that the green plane in Figures 4.6, 4.7, 4.8, and 4.9 is the minimum required gripping force to hold the weight of the aircraft while perched on surrounding infrastructure.

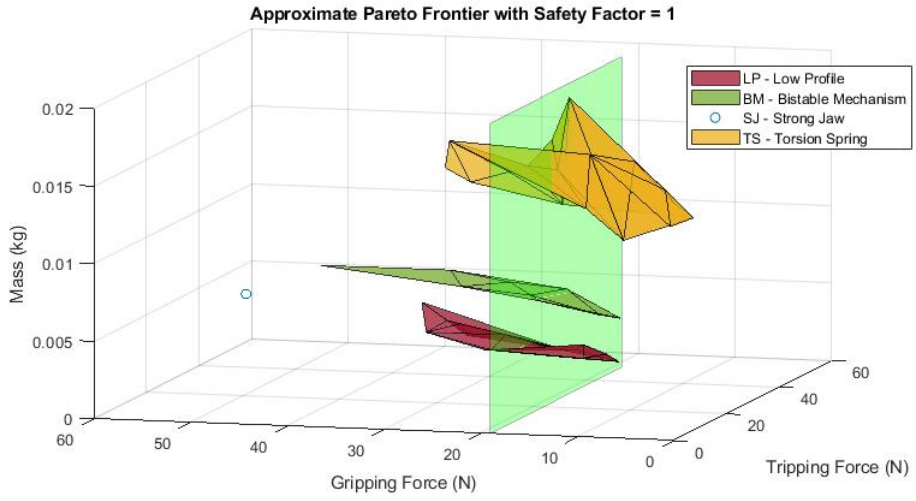

Figure 4.6: Non-dominated frontiers with respect to frontal area for LHS DOE with safety factor of 1 and no constraints.

As constraints and safety factors are applied, the non-dominated solutions begin to shrink as seen in Figure 4.7. This is a great example to explain Pareto optimality of an objective space. After constraints are applied the new non-dominated frontiers become a subset of what previously was the non-dominated frontiers in Figure 4.6.

The reduction in size is due to the violation of the maximum and minimum constraints of the gripping force and tripping force as well as violations of the yield stress of the material. Therefore, as we attempt to maximize gripping force, minimize gripping force, and minimize the lower the desired designs would be approaching the lower left corner of the objective space in Figure 4.7. Thus, with respect to the frontal area, the clear front runners are the LP and SJ mechanisms due to their lower profile designs. The affects of drag for each model will be described further in Section 4.3 before a model is selected from the DOE.

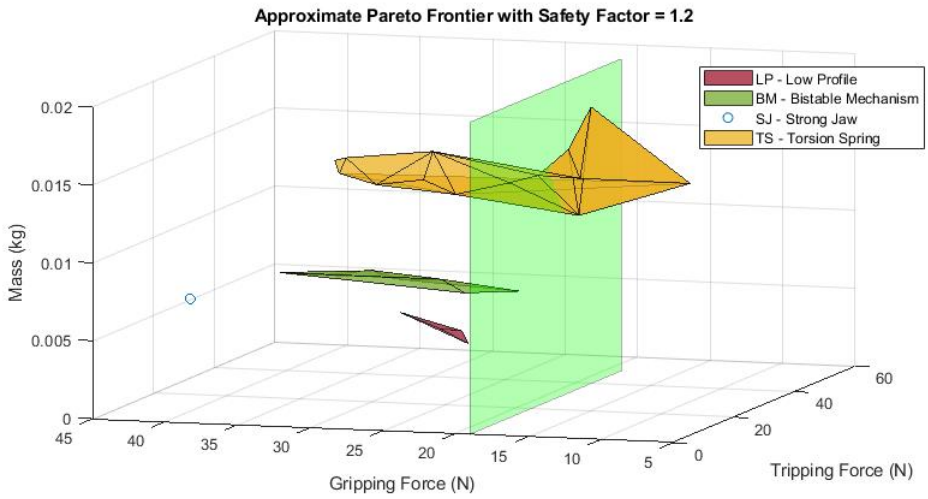

Figure 4.7: Non-dominated frontiers with respect to frontal area for LHS DOE with safety factor of 1.2 and constrained.

4.2.5.2 Gripping and Tripping Force vs. Mass

From our discussion on subsystem goals in chapter 1, we know the importance of the affect of mass/weight on induced drag due to the gripper on the aircraft. As mass increases, the induced drag due to the gripper on the aircraft increases quadratically. Therefore, minimization of mass will have a huge effect on the performance of a gripping mechanism.

The non-dominated frontier of the gripping mechanism forces with respect to mass before constraints have been applied can be seen in Figure 4.8. The favorable direction is still that of the lower left corner for these non-dominated frontiers as well. Hence, strictly with respect to mass the clear front runner for high force-to-mass ratio is that of the BM model. It accomplishes the mission goals with the lowest mass.

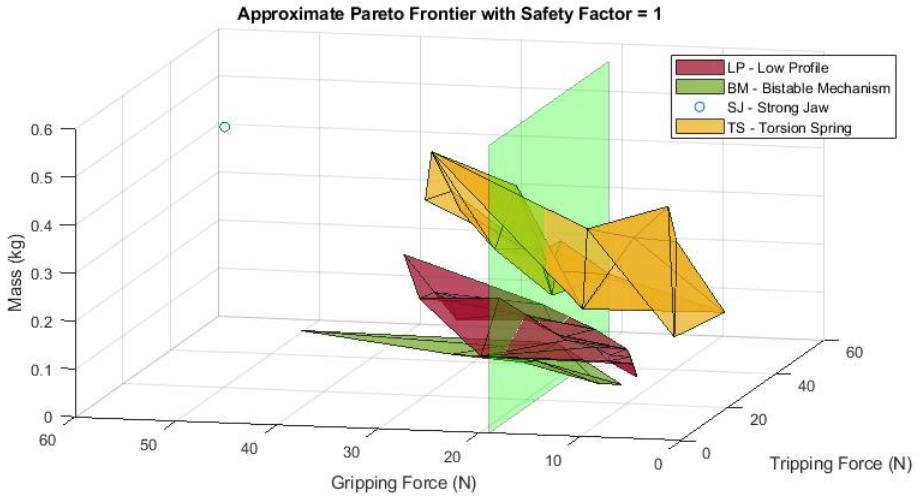

Figure 4.8: Non-dominated frontiers with respect to mass for LHS DOE with safety factor of 1.2 and no constraints.

An interesting observation that is most apparent in Figure 4.8 is that the non-dominated frontiers are intersecting. This confirms that the homogenization and parameterization efforts described in Section 4.2 yield comparable designs for the DOE.

Once constraints have been applied to the gripping force, tripping force, and mass objective space, the non-dominated frontiers shrink as a results of the maximum and minimum constraints, just as in the objective space found in Figures 4.6 and 4.7. After examining the constrained objective space, the consensus from the analysis of Figure 4.8, remains true for the non-dominated frontiers found in Figure 4.9. The gripper mechanism that achieves the highest gripping force-to-mass ratio is by far that of the BM model.

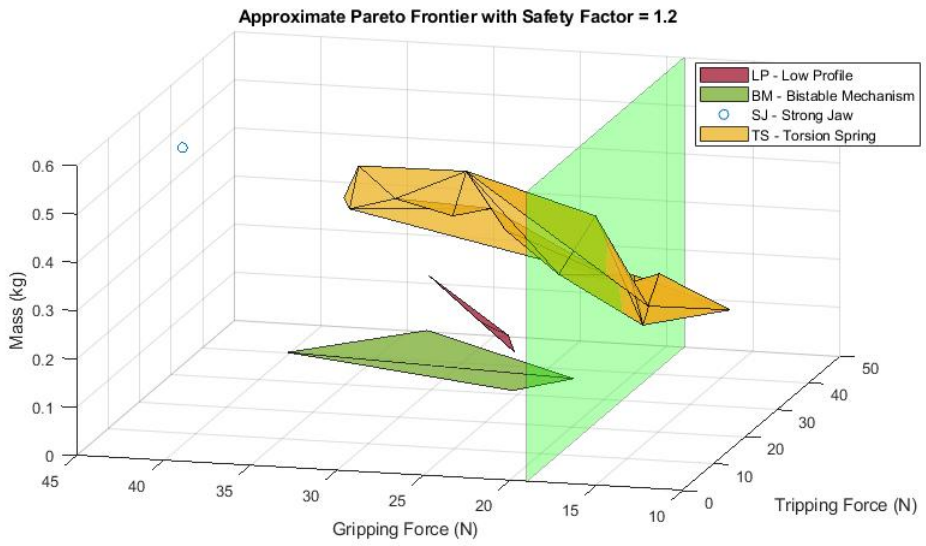

Figure 4.9: Non-dominated frontiers with respect to mass for LHS DOE with safety factor of 1.2 and constrained.

The overall concerns of the design trade study is that the BM model is the most reliable design when considering the gripping force-to-frontal area and gripping force-to-mass ratio. However, it is important to not that other factors of the drag equations have not yet been examined and could favor another design overall. The following section will discuss the down-selected process and further study the affects of drag on each of the mechanisms in the DOE.

4.3 Gripper Concept Down-selection

The following section discusses the gripper design down-selection process. Gripper drag and constraints has a significant role in the down-selection process. A more detailed discussion drag and constraints can be found in Sections 1.3 and 6.2.1. It is important to consider drag not cost to examine just the aerodynamic performance of a mechanism, because the cost can be influenced by the rewards and penalties of the constraints.

Gripping Mechanism	Tripping Force (N)	Gripping Force (N)	Gripper Drag (N)	Cost
Low Profile	25	28	0.04	-0.03
Strong Jaw	22	43	0.3	0.1
Bi-stable Mechanism	86	74	0.2	0.06
Torsion Spring	12	33	0.6	0.5

Table 4.2: LHS results comparisons for down-selection.

The designs in Table 4.2 are the optimal solutions from each LHS DOE described in Section 4.1. A quick analysis of the results in Table 4.2 yields that the low profile mechanism is the selected best design with respect to structural and aerodynamic performance. The first outlier is BM due to the fact that the tripping force of its optimal solution violates the maximum tripping force constraint ($(F_{trip})_{max} = 39N$). Although, the SJ and TS models perform favorably in terms of structural response, their aerodynamic performance is an order of magnitude higher than that of the LP model. Thus, by process of elimination the LP model is the selected gripping mechanism to be optimized for final design.

4.3.1 Low Profile Gripper Drag and Cost Analysis

The total drag coefficient assumed for the LP gripping mechanism is conservatively chosen to be similar but higher than that of a flat plate parallel to the flow. Thus, a total drag coefficient of $C_{D_g} = 0.002$ is assumed for the LP gripper.

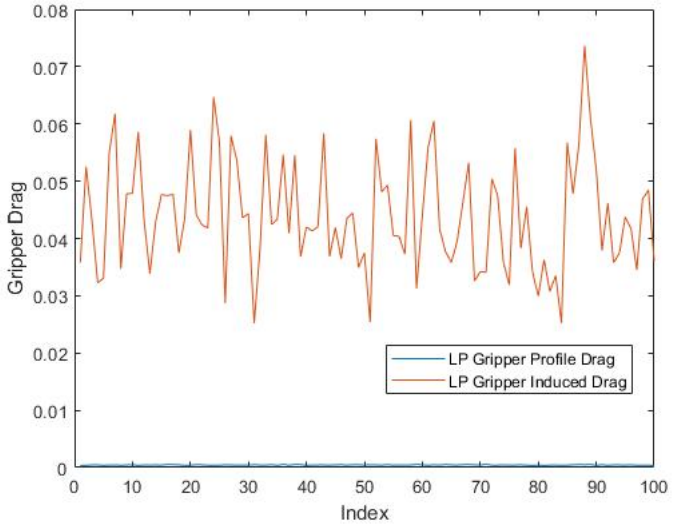

Figure 4.10: LP LHS DOE Drag Comparison.

When examining Figure 4.10, notice that the induced drag due to the mass of the gripping mechanism is significantly higher than that of the profile drag. This is due to the low profile design of the mechanism. Even with a conservative coefficient of total drag that is two times higher than that of a flat plate parallel to the flow ($C_{D_g} = 0.002$) the profile drag of the LP model is negligible.

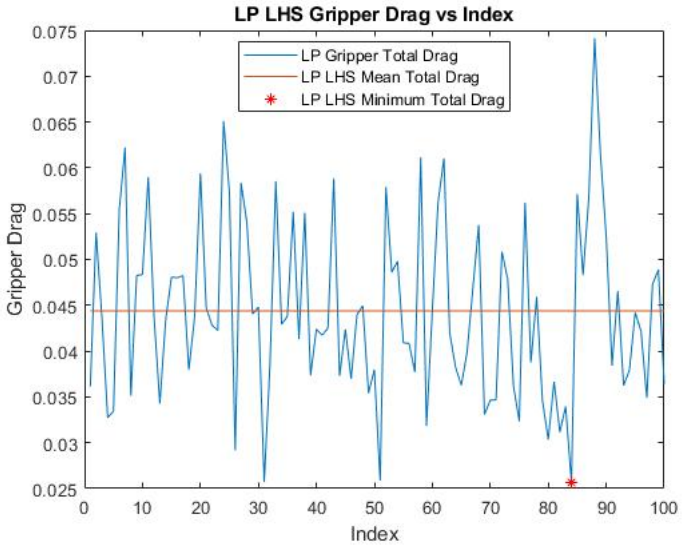

Figure 4.11: LP LHS DOE Drag vs Index.

As we further scrutinize the selected LP mechanism design, the mean drag of the 100 sample

LHS DOE from Figure 4.11 for the LP model is still significantly less than the mean total drag of the TS model.

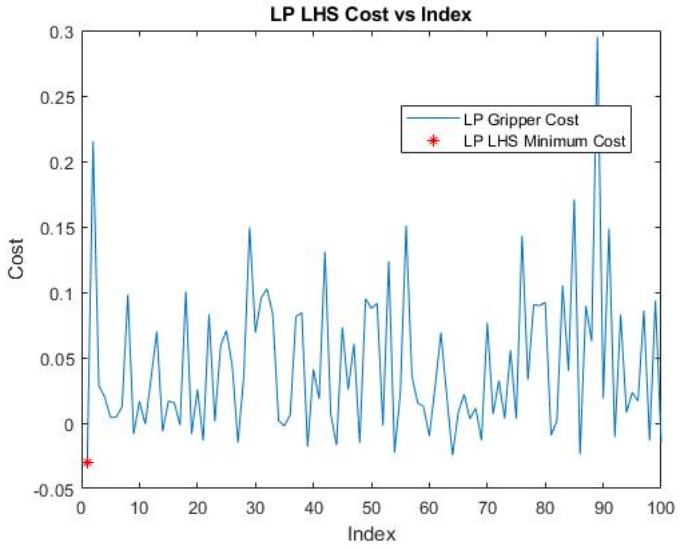

Figure 4.12: LP LHS DOE Cost vs Index.

The LP model best cost in Figure 4.12 shows that the best design is not necessarily the design with the lowest drag. The primary goal of the gripping mechanism is to carry the weight of the aircraft while perching and simultaneously trip with a reasonably low tripping force. The tripping force cannot be low enough that spontaneous gripping may occur in flight and also must not be so high that the aircraft weight and momentum cannot trip the mechanism while perching.

4.3.2 Strong Jaw Gripper Drag and Cost Analysis

The SJ model coefficient of drag is assumed to be the average of the LP total coefficient of drag and the TS total coefficient of drag ($C_{D_g} = 0.501$). The LP model is assumed to have a profile comparable to that of a flat plate while the TS model is assumed to have a profile similar to that of a flat plate perpendicular to the flow.

The assumed coefficient of drag was made qualitatively, based on the shared physical characteristics between the SJ profile and the LP and TS profiles. The SJ beam profiles resemble those of the LP model and the SJ jaws resemble the profile of the TS model.

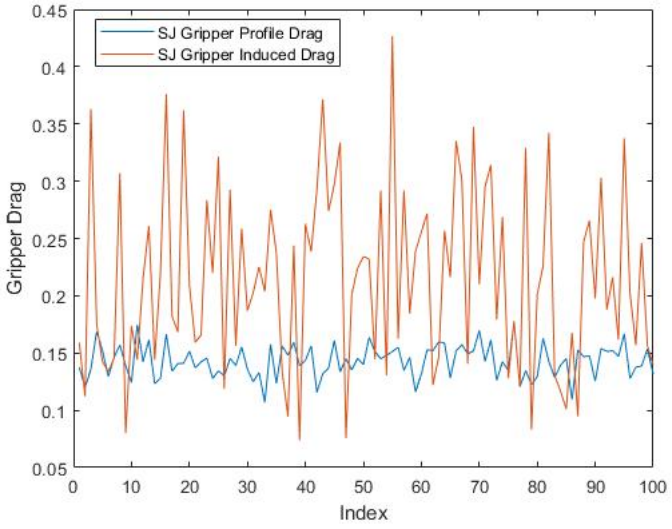

Figure 4.13: SJ LHS DOE Cost vs Index.

The high profile drag and induced drag associated with the SJ model, shown in Figure 4.15, would have eliminated the SJ model from the running regardless of the maximum tripping force error. The extra beam and jaw set that allowed the SJ to compete with the rest of the design in terms of gripping force, subsequently penalized the design with increased mass.

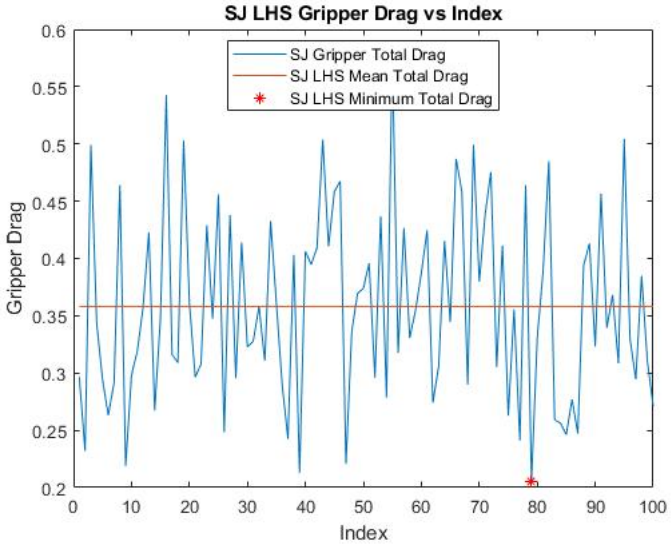

Figure 4.14: SJ LHS DOE Drag vs Index.

In addition, the mean total drag coefficient and the best total drag observed in Figure 4.14 is

significantly higher than that of the LP model.

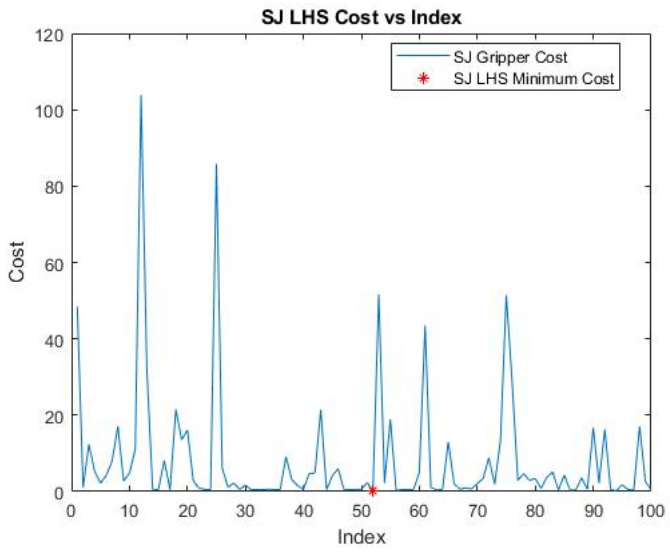

Figure 4.15: SJ LHS DOE Cost vs Index.

The best gripper design per the lowest cost of the 100 sample SJ LHS DOE represented in Figure 4.15, is still twice as high than that of the LP model. Partially due to the violation of the tripping force constraint but also due to such high drag forces.

4.3.3 Bi-stable Mechanism Gripper Drag and Cost Analysis

Similar to the assumption and calculation of the SJ coefficient of drag, the BM coefficient of drag is defined to be the same as that of SJ ($C_{D_g} = 0.501$), the average between the LP and TS coefficient of drag.

The coefficient of drag assumption was made qualitatively, based on the shared physical characteristics between the BM profile and the LP and TS profiles. The BM beam and jaw profiles resemble those of the LP model and the BM frame resemble the profile of the TS model.

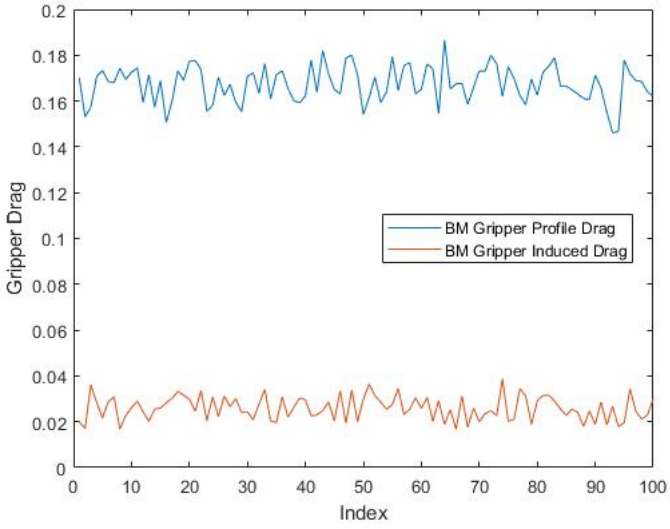

Figure 4.16: BM LHS DOE Drag Comparison.

The induced drag of the BM is observed to be low in Figure 4.16, which coincides with the observations made about the BM non-dominated frontiers in Figure 4.8 and 4.9 from the design trade study.

Although the mass and induced drag are low, the profile drag of the BM gripping mechanism is high enough to increase total drag of the mechanism significantly. Yielding a mean drag and best drag from the 100 sample BM LHS DOE that are higher than those of the LP and SJ. The previously stated trend can be observed in Figure 4.17 for the BM mechanism model DOE.

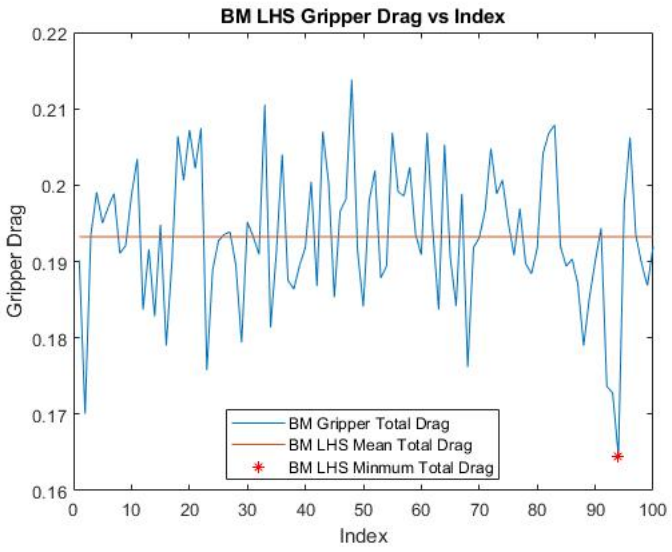

Figure 4.17: BM LHS DOE Drag vs Index.

It is interesting to conclude that the BM is eliminated due to the drag while it hold the best cost of all the mechanism, as shown in Figure 4.18 below. This is due to the fact that the BM LHS DOE discovered the highest gripping force amongst the best designs. This rewarded the primary goal of the cost function; however, the large gripping force was associated with a high tripping force that violated constraints. Thus, the BM is eliminated form the running.

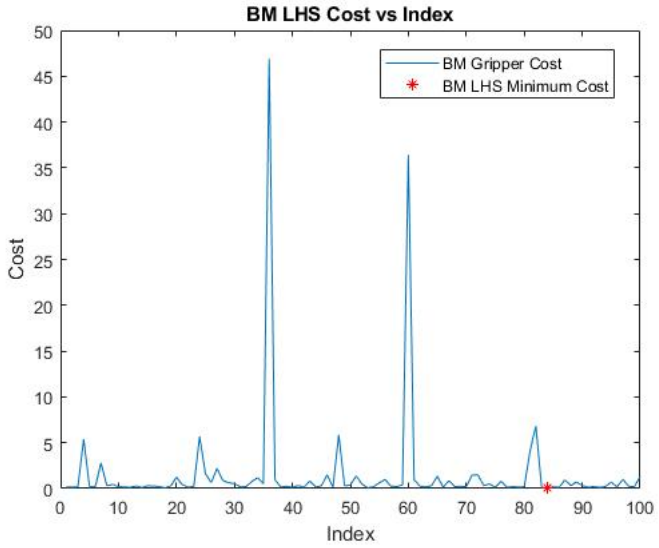

Figure 4.18: BM LHS DOE Cost vs Index.

4.3.4 Torsion Spring Gripper Drag and Cost Analysis

The total drag coefficient assumed for the TS gripping mechanism is chosen to be slightly less than that of a flat plate parallel to the flow. Thus, a total drag coefficient of $C_{D_g} = 1$ is assumed for the TS gripper as stated in the literature.

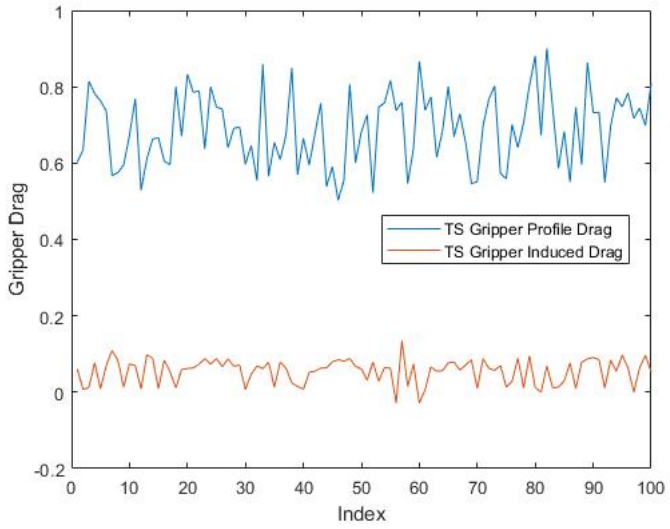

Figure 4.19: TS LHS DOE Drag Comparison.

It is no surprise that the profile drag of the TS model observed in Figure 4.19 is much higher than that of the induced drag. A greater profile drag of the heaviest gripper per the design trade study is a noteworthy finding. In Figures 4.8 and 4.9, the TS model is has the largest mass. This find tells us that the torsion spring model would benefit from a distribution of mass for structural integrity and weight saving. Especially since the TS model forces do not depend on the geometry as in the LP, SJ, and BM models. In addition, the mean drag and the best drag of the TS model are the worst among all the designs. There is not doubt that the TS will not be selected for optimization.

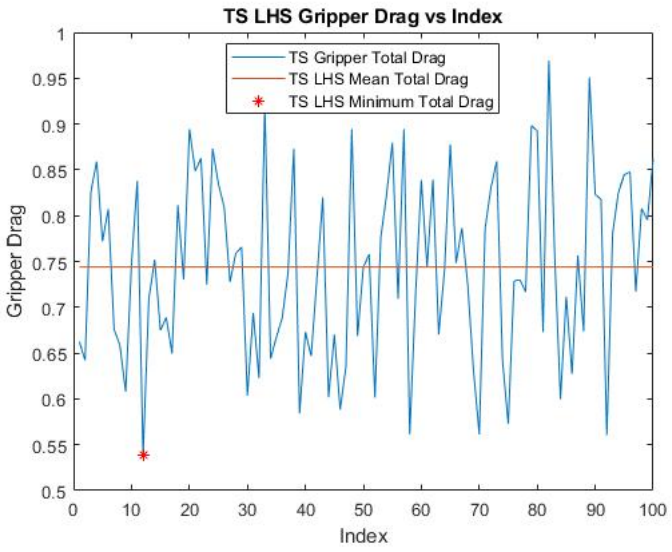

Figure 4.20: TS LHS DOE Drag vs Index.

The cost evolution over the 100 sample TS LHS DOE re-iterates the previous conclusions. The TS model has the worst cost amongst all design, as shown in Figure 4.21.

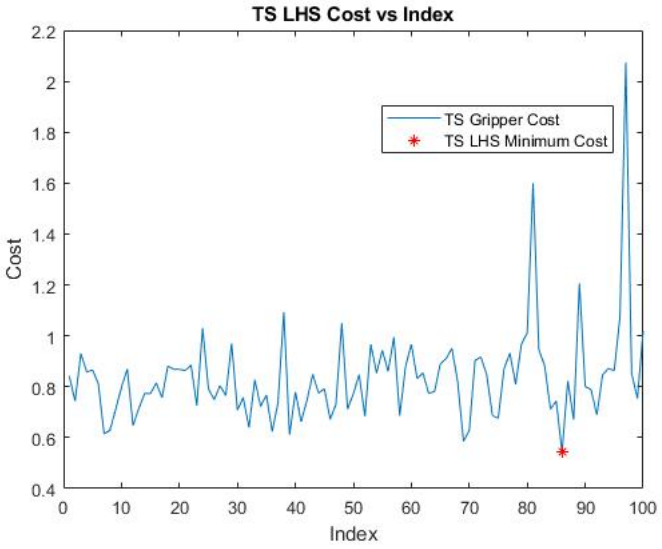

Figure 4.21: TS LHS DOE cost vs Index.

5. PROTOTYPING TESTING AND VALIDATION

The following sections highlight an active perching demonstration with the low profile model and describes the results of all the tests performed for each of the gripping mechanisms. The goal of any design study is to reach a final design for service in the field. Thus, finite element model simulations must be fabricated and replicated via experiments in order to ensure that the physics of the problem has been accurately simulated.

5.1 Model Testing Overview

In this work, the four gripper designs require tripping and gripping experiments to validate the Abaqus FEA. From the experiments we have learned that the quasi-static time integration technique discussed in Chapter 3 is an acceptable preliminary design study that compares the performance of the different mechanisms. Quasi-static models allow us to compare designs without considering additional physical phenomena (e.g., friction, material damping, etc.) required to dissipate energy from the system. However, future work must consider more robust methods of time integration to more accurately simulate the dynamic behavior of the selected gripping mechanism for the final design.

Abaqus/Standard implicit offers a moderate dissipation integration technique as an alternative to quasi-static integration. While implementing Abaqus/Standard implicit schemes validation experiments prove that such dynamic events (e.g., impact) require more fidelity than the quasi-static solver can offer. Although a moderate dissipation integration technique would yield more accurate results for the analysis, convergence issues could arise. With less numerical energy dissipation and smaller time steps the moderate dissipation time integration technique would capture the dynamic events of the system more accurately, but would require additional energy dissipation consideration in order to converge to a solution. Further study is required to implement the effects of friction and material dampening for designs of experiment that can consistently converge to a solution while using moderate dissipation for dynamic FE models, such as the mechanisms in this work.

Validation data was acquired through tripping and gripping experiments for each mechanism. The gripping force and the tripping force for each model were evaluated using an Imada FB-10 analog mechanical force gauge and recording on a mobile phone to capture the values. The mechanical locking feature of the gauge was used to record peak force measurements for all of the experiments. The tripping and gripping force test results for each model are compared against their FEA results from the Abaqus models described in Sections 3.1, 3.2, 3.3, and 3.4. These experiments are seen in Sections 5.2, 5.3, 5.4, and 5.5, one for each model. The validation results highlight the differences between the physics of an ideal simulated environment and that of reality.

Updated validation models that reflect the discrepancies between the FE models and the validation prototypes are referred to as Match FEA models. Match FEA models that implement quasi-static or moderate dissipation time integration will be referred to as QS Match FEA and MD Match FEA, respectively.

Model		Tripping Force (N)	Gripping Force (N)
Low Profile	Validation	4.72	8.94
	MD Match FEA	5.62	7.93
	MD Match Error	19%	-11%
Strong Jaw	Validation	4.18	6.72
	MD Match FEA	4.79	4.42
	MD Match Error	15%	-34%
Bi-stable Mechanism	Validation	16.41	5.74
	MD Match FEA	10.93	5.92
	MD Match Error	-33%	3%
Torsion Spring	Validation	4.67	14.5
	MD Match FEA	5.54	16.9
	MD Match Error	19%	17%

Table 5.1: Final Match FEA validation results.

Table 5.1 depicts the differences due to manufacturability as well as FE model assumptions.As

expected, discrepancies arise after fabrication and assembly due to supplies and manufacturing techniques. However, once the discrepancies between the FE models and the validation prototypes are addressed and moderate dissipation time integration is implemented, the models accurately represent the results of the validation experiments.

5.1.1 Elastic Modulus Validation

A Markforged 3D printer is used to print all the prototypes from Markforged Onyx material. To ensure the material properties are accurately represented in the FE simulations, the model is calibrated using a beam from a validation prototype. The 3D Onyx beam was taken from the LP validation prototype to be cantilevered and used for elastic modulus validation as shown in Figure 5.1.

Figure 5.1: Elastic Modulus Validation Experiment.

The cantilever beam is 13.5 cm long, 3.55 cm wide, and 5.88 mm thick with a 100% infill print. A dial gauge was setup near the mid-span of the beam to measure deflection in the y-direction. For the validation experiment, a deflection of 0.54 mm is measured after a mass of 134.9 grams was hung from the tip of the beam. When compared with the results of the virtual experiment, it was

clear that the Onyx material properties provided by Markforged are incorrect as shown in Section 5.3.

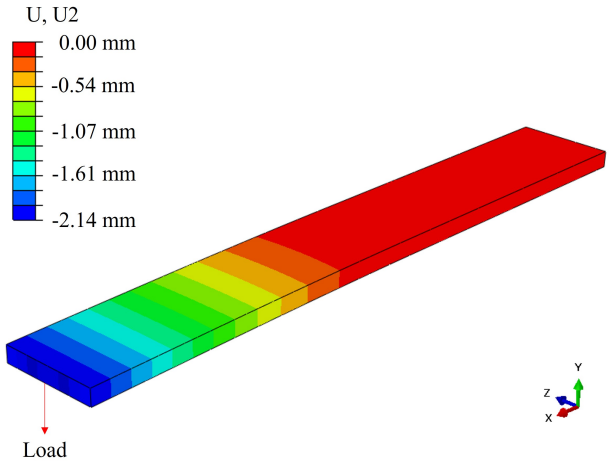

Figure 5.2: Elastic Modulus Validation Experiment.

The same experiment was performed using Abaqus FEA with the material properties provided by Markforged, as can be seen in Figure 5.2. A beam of the same dimensions was cantilevered in Abaqus with an equivalent concentrated force of 1.32 N applied to the center-tip of the beam. With an elastic modulus of 2.4 GPa, as stated by the Markforged, the measured y-displacement of the beam at the same point as the dial gauge was 0.18 mm. The modulus was then incrementally changed until the FE displacements matched the validation experiment values. The resulting elastic modulus for a matching displacement of 0.54 mm was found to be 0.82 GPa for Markforged Onyx material.

It is important to note that the Abaqus FEA models do not include initial plastic deformation or fatigue and the beam used in experimentation has gone through tens of experiments. Onyx seems to weaken significantly in only 1 to 2 cycles. The effects of creep on the strength of such a material are noticeable in some of the validation experiments and will be discussed in the following sections.

5.2 Low Profile Model Testing

The data collected from LP tripping and gripping experiments is shown in Table 5.2. It is clear that some discrepancies between the FE and validation models need to be addressed. Due to such high tripping and gripping force errors, changes must be made to account for manufacturing methods, supplies, and modeling assumptions. The forces depend highly on the kinematics involved with rotation about the 3 hinges of the model. Therefore, the DOE model shown in Figure 5.3 must be updated to reflect the spacing between the beams and jaws due to the presence of the hinges. The DOE FEA model is representative of the low profile FE model described in Section 3.1 and used for DOE in Chapter 4.1.

Figure 5.3: Low Profile DOE FEA model.

The DOE FEA model was built before the hinges for the validation prototype were purchased. The only hinges available did not meet the expectations of the initial design of the LP model. The Match FEA model shown in Figure 5.4 is reassembled to include spacing between the beam and the jaws due to the validation prototype hinges.

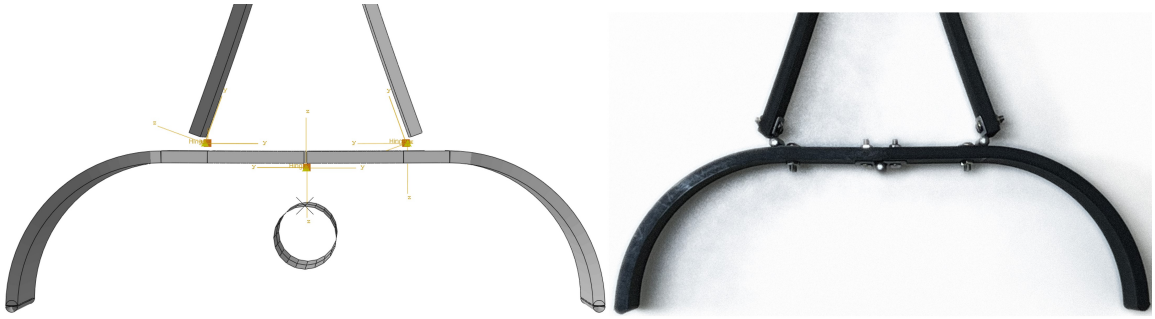

Figure 5.4: Low Profile Match FEA model.

The QS Match FEA model in Table 5.2, shows that the adjustments made to account for manufacturability reduced the gripping force error. However, the high tripping force error can be attributed to a dynamic aberrations that quasi-static time integration was not able to capture. The MD Match FEA model represents the same model with moderate dissipation time integration implemented. With the addition of moderate dissipation time integration, the tripping force error becomes reasonably low while also further reducing gripping force error. The results of the experiments in Table 5.2 further emphasise that high energy dissipation and time steps are not sufficient for the analysis of such dynamic behavior, we must also quantify instantaneous events. We have made progress but follow-on work will have to be more careful in assessing values that are only measurable in small amounts of time.

Model	Tripping Force (N)	Gripping Force (N)	Time Integration Technique
Validation	4.72	8.94	
DOE FEA	1.68	4.10	Quasi-static
DOE Error	-64%	-54%	
Validation	4.72	8.94	
QS Match FEA	9.56	7.65	Quasi-static
QS Match Error	103%	-14%	
Validation	4.72	8.94	
MD Match FEA	5.62	7.93	Moderate Dissipation
MD Match Error	19%	-11%	

Table 5.2: Low profile model validation data.

5.2.1 Low Profile Tripping Force Validation

The tripping force experiments were performed with an Imada FB-10 analog mechanical force gauge and can be seen in Figure 5.5. The low profile model assembly was fixed at the top of the beam using a clamp. The gauge was attached to an aluminum plate that was wedged in between two aluminum beams. The beams are bolted to a work bench and act as guide rails to keep the aluminum plate and the force gauge straight. The aluminum plate is then attached to a lead screw

that controls the axial position of the force gauge. The low profile model was positioned perpendicular to the gauge in its open state, as shown in Figure 5.5. The gauge is then pushed through the middle hinge of the low profile assembly until the mechanism is tripped and closed. Two bolts are threaded into the table on either side of the gauge tip to ensure that the gripper does not grip the gauge and affect the final reading.

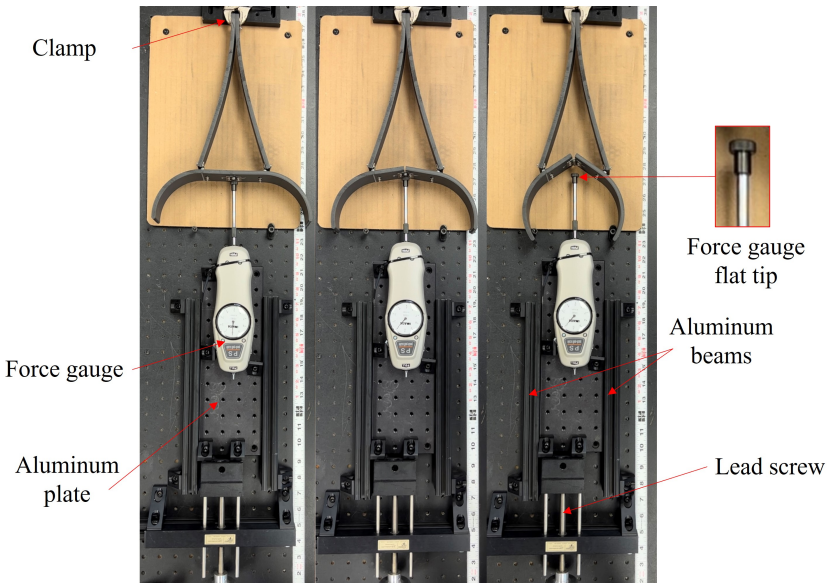

Figure 5.5: Low Profile Tripping Experiment.

The previous results of the validation show that the tripping force from the DOE FEA is significantly lower than experimentally measured. This is due to the fact that the DOE FEA model assumes the center of the middle hinge is at the top edge of the jaw, in line with the left and right hinges. The position of the middle hinge directly affects the tripping force of the mechanism. From Section 4.2.1, a design variable called the *stop angle* is described to increase the reaction moment due to the strain energy stored in the deflected beams and increase the tripping force. The validation prototype assembly as shown in Figure 5.5 has an induced *stop angle* greater than zero (the neutral point is at a *stop angle* of zero). The only hinges available for such a small assembly were 270° hinges rather than 360° which would have impeded the middle hinge's ability to allow the jaw to close. Therefore, the hinge was installed between the bottom edge of the jaws. For similar reasons, the two side hinges as shown in Figure 5.4 were also placed on the inner edges of

the beams, to allow full rotation of the jaw. The additional spacing between parts due to the new hinge setup increased the maximum deflection of the beams in addition to inducing a *stop angle*, both of which increase the strain energy storage and tripping force of the mechanism.

Additionally, DOE, QS Match and MD Match FEA models assume that all three hinges are frictionless, which is not the case in reality. Both differences would lead us to assume that the tripping force in the validation would be higher than in the FEA. The tripping force in the validation experiment had to overcome a larger reaction moment than in the DOE FEA due to the induced *stop angle*, increased maximum deflection of the beams, and the friction forces in all three hinges.

5.2.2 Low Profile Gripping Force Validation

The gripping force experimental setup remains the same except for a few differences. The new setup requires the gripper to be initially in the closed state with a rigid cylinder inside the grip, representing the power line. The force gauge tip is changed from a flat tip to a hook as shown in Figures 5.5 and 5.6. The gauge lead screw is then rotated in the opposite direction to pull the gripper assembly out from around the power line. The maximum force measured with the gauge while pulling the gripper from the end of the beams is defined as the gripping force.

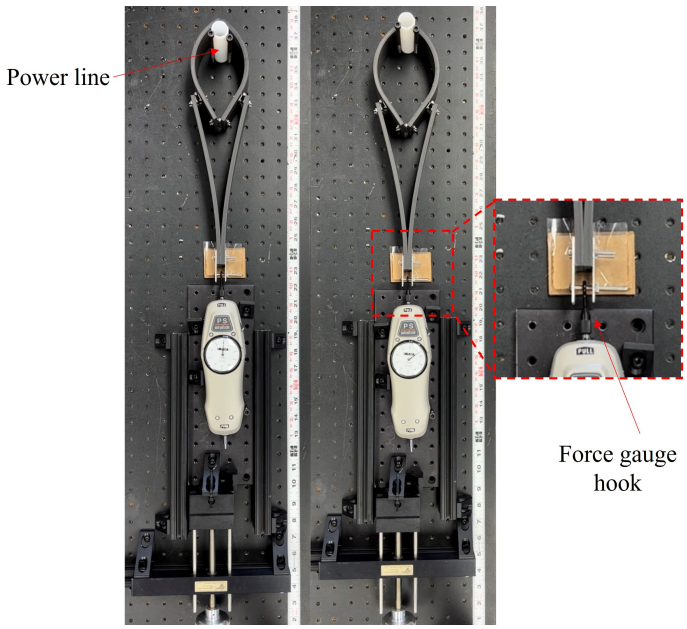

Figure 5.6: Low Profile Gripping Experiment.

The results from Table 5.2 show that the gripping force from the DOE FEA is lower than the results of the validation experiment. Similar to the discussion about the tripping force, the gripping force is also affected by the induced *stop angle* due to the discrepancy in the hinge setup between the validation prototype and the DOE FEA. In addition, the effects of friction are not accounted for in the FE models.

5.3 Strong Jaw Model Testing

The strong jaw model experimental setup was similar to the low profile setup due to their related geometry, but proved to be a more challenging model to test. The SJ jaw and beams are offset from each other, making it hard to lay the mechanism level on a table for testing. An offset jig is required to hold the beams level and can be seen in Figures 5.7 and 5.8. From Table 5.3 the error associated with the DOE FEA model does not support the assumptions made in the simulations. FE models are perfectly parallel, perpendicular, and frictionless which would yield lower forces for tripping and gripping. The differences between the Match FEA model and the validation support such a trend. Moreover, the material system used for prototyping is not a reliable material for repeated dynamic testing. The following subsections will describe such discrepancies in depth along.

Model	Tripping Force (N)	Gripping Force (N)	Time Integration Technique
Validation	4.18	6.72	
DOE FEA	19.7	9.38	Quasi-static
DOE Error	370%	40%	
Validation	4.18	6.72	
QS Match FEA	6.22	5.13	Quasi-static
QS Match Error	49%	-24%	
Validation	4.18	6.72	
MD Match FEA	4.79	4.42	Moderate Dissipation
MD Match Error	15%	-34%	

Table 5.3: Strong jaw model validation data.

5.3.1 Strong Jaw Tripping Force Validation

Similar to that of the low profile tripping force experiment, the strong jaw model was positioned perpendicular to the gauge tip, in the open state. The gauge was pushed up against the jaw using a lead screw, while the gripper was bolted to an offset jig to fix the assembly at the top of the beams. The maximum force measured by the gauge while pushing the gauge through the center hinge is defined as the tripping force. The three major steps of the experiment are shown in Figure 5.11.

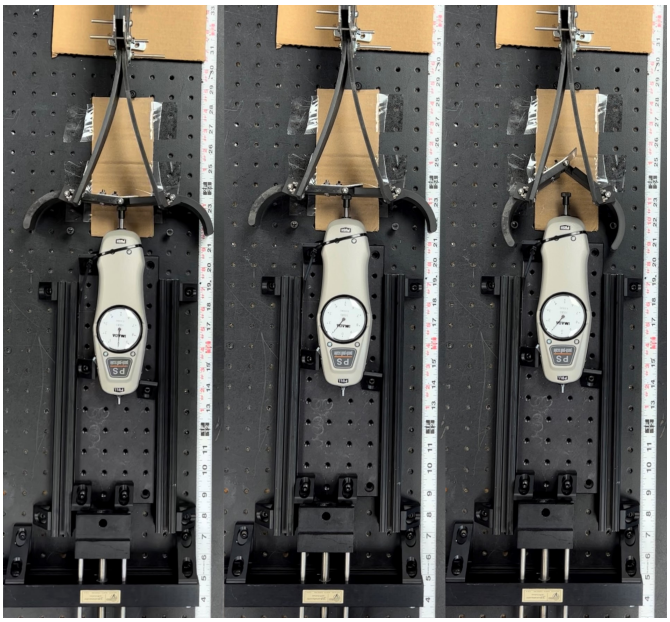

Figure 5.7: Strong Jaw Tripping Force Experiment.

A major difference between the FE model and the validation is the symmetry boundary conditions. The FE model has symmetry boundary conditions that balance out the moments caused by a jaw that is offset from the bending beams that drive the mechanism. In the validation, only half of the strong jaw model was tested due to difficulty tripping and gripping the two offset jaws simultaneously. A more elaborate experimental setup is needed for testing the full strong jaw model in the future. Therefore, to make the validation and the FEA match, the strong jaw Match FEA models are simulated without symmetry boundary conditions. Both QS Match FEA and MD Match FEA do not include symmetry boundary conditions.

The strong model joints are modeled as frictionless hinges in the FE model, while the validation

model was built without hinges or bearings. Instead, the validation model jaws rotate about a threaded bolt inserted through a pre-printed hole in the Onyx jaw structure, which had 100% infill. Friction force increases proportionally with the its associated normal force component. Tripping force is required to overcome the neutrally stable point of the gripper mechanism, at which beam deflection and in turn forces are their maxima. As opposed to gripping force where the jaws are closed and the beams significantly less deflected. Thus, higher tripping force error can be associated with amplified frictional forces due to higher normal force.

5.3.2 Strong Jaw Gripping Force Validation

The gripping force experiment required the mechanism to be set in the closed state with a rigid cylinder inside the grip to represent the power line. The maximum force measured with the gauge while pulling the gripper out from around the cylinder is defined as the gripping force.

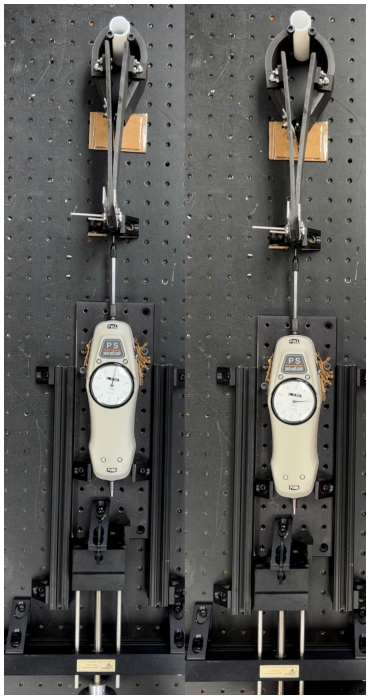

Figure 5.8: Strong Jaw Gripping Force Experiment.

Similar to the reasons mentioned in the previous section, the gripping force measured in validation is different than found in the FE model due to friction, hinge assembly, gripper assembly, creep, and experimental error. The strong jaw model has added complexity and error in gripping

force experiments as opposed to its tripping force experiment. For this experiment the gauge is hooked to the top of the beams, where the offset jig is holding the beams level. While pulling the gripper, the offset jig and the SJ assembly are dragged along the surface.

Due to the offset between the gripper jaws and beams, equal and opposite moments about longitudinal axis of the two beams is induced. This leads to threaded bolts in the validation prototype hinges that are no longer concentric with the through holes they are inserted into. Strain energy is lost to the moment about the beams, causing a reduction in gripping force for the Match FEA models. In addition, the moments from the offset may have lead to higher force due to friction than in the DOE FEA simulations that consider symmetry boundary conditions. Given that half the validation prototype is missing from both the tripping and gripping experiments and the simulations is considering the whole mechanism, the FEA models behave as expected.

5.4 Bi-stable Mechanism Model Testing

The bi-stable mechanism experiments were not very different than the LP and SJ experiments in that a similar experimental setup could be used. The boundary condition of the DOE FEA model assumed that the entire top surface of the mechanism was fixed in all directions using an analytically rigid surface in contact with the top surface of the frame, as shown in Figure 5.9 and discussed in Section 3.3.

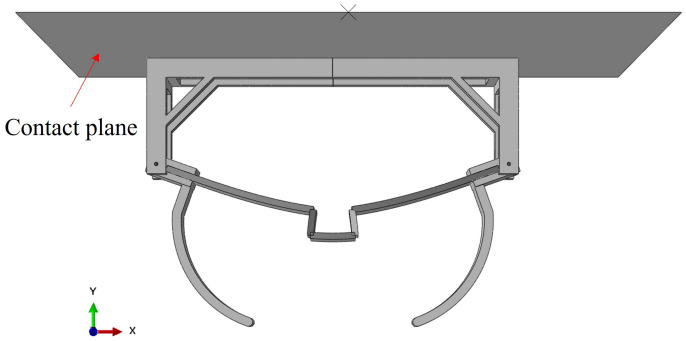

Figure 5.9: Bi-stable Mechanism DOE FEA model.

This assumption is acceptable when the gripping mechanism is mounted to the aircraft. However, a validation study incorporating the fixed top surface would have complicated the experimental setup considerably. For comparison with the validation at hand, the fixed top surface boundary condition in the DOE FEA model was replaced with a new boundary condition for the Match FEA model.

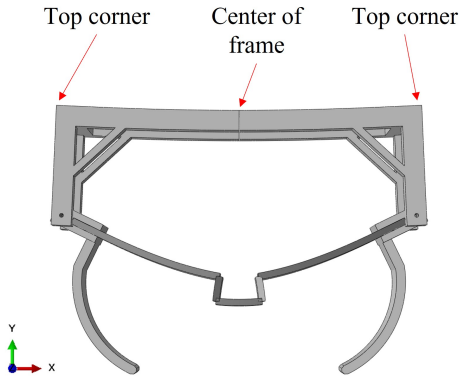

Figure 5.10: Bi-stable Mechanism Match FEA model.

The new boundary conditions fixed the top center of the frame and allowed the top corners to displace in the x and y-direction and rotate about the z-axis as shown in Figure 5.10. The validation test results are compared to both the DOE FEA model and the Match FEA models and can be found in Table 5.4.

Model	Tripping Force (N)	Gripping Force (N)	Time Integration Technique
Validation	16.41	5.74	
DOE FEA	10.98	6.21	Quasi-static
DOE Error	-33%	8%	
Validation	16.41	5.74	
QS Match FEA	12.17	6.57	Quasi-static
QS Match Error	-26%	14%	
Validation	16.41	5.74	
MD Match FEA	10.93	5.92	Moderate Dissipation
MD Match Error	-33%	3%	

Table 5.4: Bi-stable mechanism model validation data.

Holistically, the tripping and gripping force error decreased as the Match FEA models were refined. The following sections will describe the tripping and gripping force experiments further and provide an explanation for the error data in Table 5.4.

5.4.1 Bi-stable Mechanism Tripping Force Validation

The validation test for the tripping force of the BM required a wall and pin to keep the boundary condition described in Figure 5.10 to keep the gripper in-line while the gauge pushed up against the compliant join of the bi-stable beam. The gauge pushing up against the compliant joint simulated the power line pushing up against the compliant joint in the FE simulation. The beam was pushed past its neutral point until it tripped toward its second stable state. These steps can be seen in Figure 5.11.

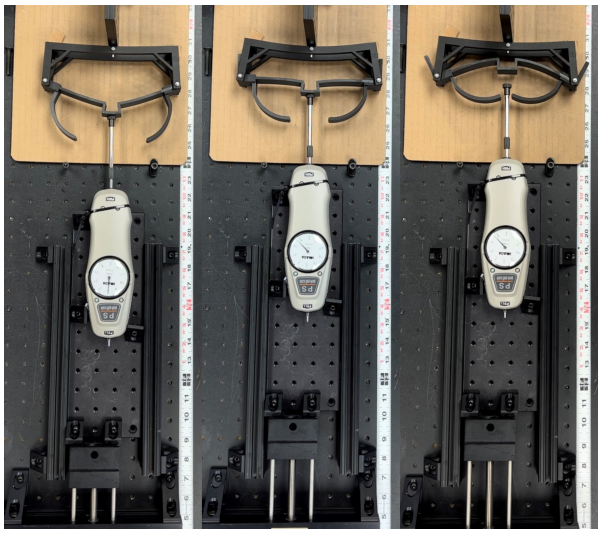

Figure 5.11: Bi-stable Mechanism Tripping Force Experiment

The tripping force is lower in the FE model for three reasons: the compliant joint in the FE model is offset to enable beam buckling at lower stresses, the FE model jaw rotates about hinges, and the FE model is frictionless. The validation bi-stable mechanism assembly does not have any bearings or hinges. Instead, the silicon-based jaw rotates about a threaded bolt in a through-hole. In addition, both jaws are wedged between their corresponding two arms of the frame. Upon rotation, the contact area between the jaw and the frame arms rub against each other. This friction contact is not modeled in the FE simulation. However, all necessary step were taken to avoid the addition of friction to the results in the validation experiments. All surfaces that come in contact with each other were sanded down and all holes were drilled for extra clearance. In addition, WD-40 was sprayed into the holes and on the contact surfaces to help reduce the affects of friction.

One additional significant factor that could be playing a role is beam buckling. Beam buckling phenomena are not straight forward to model using FE methods. Buckling phenomena are mathematically singularities that would require further study. Especially since the elastic modulus validation in Section 5.1.1 confirmed that we cannot confidently predict the effects of creep and fatigue of Onyx.

5.4.2 Bi-stable Mechanism Gripping Force Validation

The validation experiment for the gripping force required holes in the top center of the frame's beams as shown in Figure 5.10. A bolt threaded into the top of the frame allows for the hook tip of the force gauge to pull the jaws out from around the rigid cylinder as shown in Figure 5.6. This most accurately represents the FE boundary conditions that held the frame fixed at the center of top center of the frame as shown in Figure 5.10.

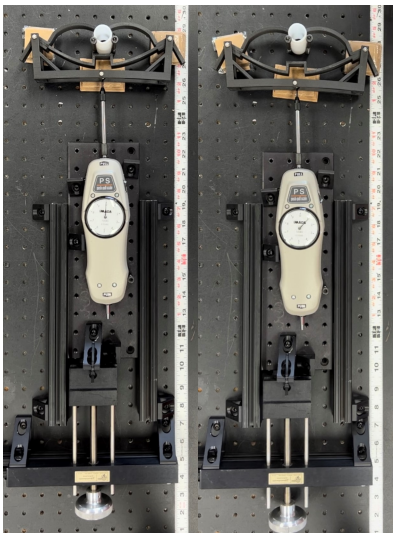

Figure 5.12: Bi-stable Mechanism Gripping Force Experiment.

All error attributed to the frictional effects, the rotations without a bearing or hinge, and the buckling phenomena approximations apply for this test as well; however, deformation of the frame likely played a large role in the additional gripping force error. This could be a direct impact from the error associated with the elastic modulus validation in Section 5.1.1. A higher modulus in the FEA could yield to a more rigid frame with a a higher gripping force.

5.5 Torsion Spring Model Testing

The torsion spring validation error consistently decreased as the FE model assumptions were refined. The TS model does not require a Match DOE model to address discrepancies due to manufacturability; however, it does still require a Match model that addresses the time integration technique used as discussed in the overview of Chapter 5.

Model	Tripping Force (N)	Gripping Force (N)	Time Integration Technique
Validation	4.67	14.46	
DOE FEA	6.74	18.4	Quasi-static
DOE Error	44%	27%	
Validation	N/A	N/A	
QS Match FEA	N/A	N/A	N/A
QS Match Error	N/A	N/A	
Validation	4.67	14.46	
MD Match FEA	5.54	16.9	Moderate Dissipation
MD Match Error	19%	17%	

Table 5.5: Torsion spring model validation data

The data in Table 5.5 shows that the FE model validation yield results that are to be expected given the material system used and the assumptions made while building the models.

5.5.1 Torsion Spring Tripping Force Validation

The torsion spring tripping experiment required the mechanism to be in an open state and perpendicular to the gauge. Similar to the boundary condition discussed for the BM, shown in Figure 5.10, the top center of the frame is fixed using the same wall and pin experimental setup. This can be seen in Figure 5.13. This experiment required bolts on either side of the gauge tip to keep the jaws from coming into contact with the gauge while closing. The gauge was pushed up against the mechanism at the middle hinge using the same lead screw setup from all experiments in this work until the mechanism tripped. The maximum force measured by the gauge while tripping

is defined as the tripping force, as shown in the middle image of Figure 5.13.

This TS error can be attributed to the effects of friction between the Onyx components in the mechanism, friction between the threaded bolts inserted in the Onyx through holes, and creep of the complaint silicon matrix.

Friction contact is not included in the FE models, making it easier for the gripper to open and close while tripping and gripping. Similar to the BM and SJ mechanisms, the real-life jaws rotated about threaded bolts which led to high friction and resistance.

Onyx is a compliant material that significantly weakens after repeated deformation. The thin walled frame of the TS model deform significantly under the constant load of the torqued torsion spring. This may amplify the affects of friction, keep the mechanism from rotating freely about its hinges, and create a mismatch in material performance between the validation prototype and the FE models. Like the SJ validation prototype, the moments could lead to non concentric bolts in their respective through holes. Again, the model assumes all that the material is pristine and is deformed for the very first time, while the validation prototype experiences significant deformation upon assembly and initial torque of the torsion springs. This could lead to reductions in material strength before initial validation experiments.

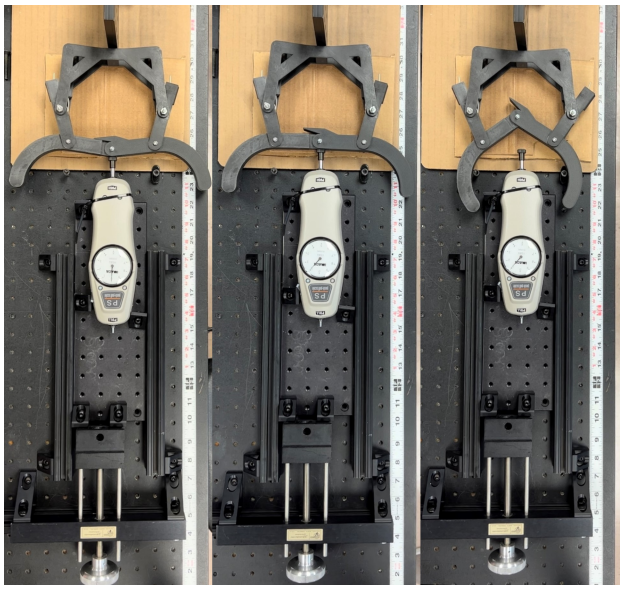

Figure 5.13: Torsion Spring Tripping Force Experiment.

5.5.2 Torsion Spring Gripping Force Validation

The torsion spring gripping force experiment required the jaw in a closed initial state with a rigid cylinder at the center to simulate the power line. A gauge hooked to the top center of the gripper was slowly and consistently pulled out from around the power line. The maximum gripping force measured by the gauge as the gripper was pulled out from around the wire is defined as the gripping force. This experiment is depicted in Figure 5.14.

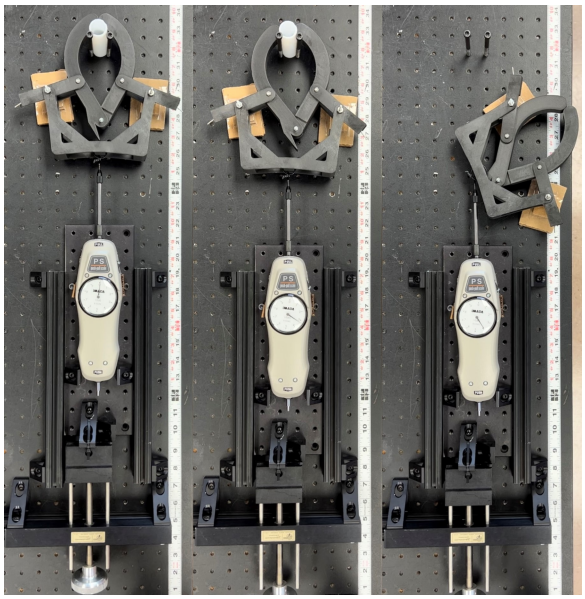

Figure 5.14: Torsion Spring Gripping Force Experiment.

The justification of the gripping force experiments is similar to that of the tripping force experiments. The experiment results are as expected and the error can be improved upon in future work with the consideration of new material systems, hinges or bearings for the validation prototype, and more robust time integration techniques for the FE models.

5.6 Active Perching Demonstration

A scale model of the low profile gripping mechanism was manufactured and assembled to demonstrate active perching, as shown in Figure 5.15. The deliverable gripping mechanism is required to provide a significant enough gripping force to overcome the weight of the aircraft. The active material actuator will have to overcome a gripping force high enough to carry the weight of

the aircraft in order to reset the mechanism.

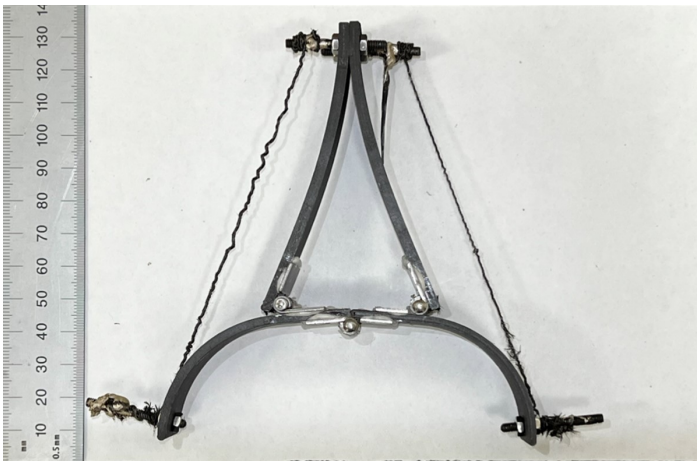

Figure 5.15: Active perching demonstration assembly.

Taking these performance requirements into consideration, a low profile mechanism design with a gripping force of 36N was selected, which corresponds to an 8N reaction force on the active material on each side of the gripper. The down-selection process that lead to the low profile mechanism scaled down for this discussed in Chapter 4.1. The fabricated polymer actuators are approximately 14.5 cm in length and can withstand up to 4 N of load each. After being scaled down to 45%, the selected gripper design subjected the polymer actuator to 3.6N of load and required a polymer actuator with no more than 12.13 cm of reference length. Using set screws, the polymer actuators were installed from tip-to-tip on either side of the gripper as shown in Figure 5.15. The set screws were also used to wind out any slack in the actuators.

To actuate the polymer material, a potential difference was induced across the actuator by connecting a power source to both set screws on either side of the actuator. Alligator clips were used to connect the corresponding set screws on the second set of actuator set screws in parallel for an equivalent potential difference across both actuators. The polymer actuator generated enough strain to reset the gripping mechanism, as shown in Figure 5.16.

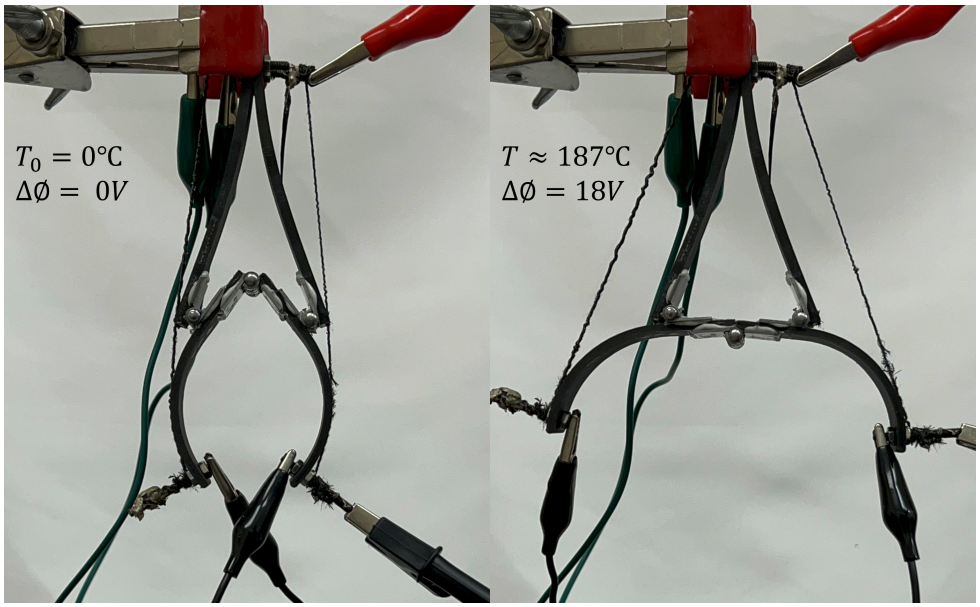

Figure 5.16: Active perching demonstration.

The image on the left shows the LP gripper in the closed state with the active material actuator in its reference state. The image on the right shows the gripper in the open state due to an electric potential stimulus of 18 V across the polymer actuator. In the reference state, the polymer actuator temperature is $T_0 = 0°C$, while the temperature in the stimulated state is about $T \approx 182°C$.

6. OPTIMIZATION

6.1 Efficient Global Optimization (EGO)

Numerous optimization schemes could be implemented to search the design space of expensive black box optimization functions. In this work a *MATLAB surrogate modeling toolbox* built by *Mueller et al.* [13] is used to fit surrogate models to the initial data produced in the design space and implements various sampling techniques to predict future candidates for the optimizer to evaluate. This work will implement Latin hypercube sampling and optimize via efficient global optimization in pursuit of the global minimum in the design space.

In similar works [14, 15], EGO is used because it applies the Kriging model to fit the initial input and output data for surrogate model training. Kriging is a statistical method of spatial interpolation based on Gaussian processes that allows the optimizer to search for the best linear unbiased prediction at unsampled locations [16]. This scheme is more efficient than simpler optimization methods (e.g., random walk).

In this work, a surrogate response surface is fit to the 100 sample LHS from the DOE to train an initially surrogate model for the optimization. Once the candidate has been evaluated, the initial surrogate response surface is updated and the next candidate is selected similarly.

An efficient global optimization (EGO) algorithm from *Jones et al.* [17] is implemented with an initial surrogate training set composed of the LHS data. EGO decreases uncertainty of the surrogate fit as it searches the design space for an optimal solution in unsampled locations of the design space. Another advantage of EGO is that it does not just exploit the design space to decrease uncertainty, it also explores the design space. The algorithm does not rely on previous data to sample the design space, it uses statistics based sampling to predict future candidates for design space exploitation.

6.2 Inputs, Outputs, and Design Optimization Statement

Low Profile Gripping Mechanism Design Optimization Problem	
Minimize:	
	Total drag due to the gripper, D_g
	Tripping force, F_{trip}
Maximize:	
	Gripping force, F_{grip}
by varying *inputs*:	
	Beam Length, L_B
	Beam thickness, t_B
	Beam width, W
	Jaw thickness, t_J
	Jaw width factor, F_{WJ}
	Beam-jaw attachment point, L_{BJ}
	Stop angle, θ
Subject to constraints on *outputs*:	
	$W_{ac} < F_{grip} < 4W_{ac}$
	$\frac{1}{2}W_{ac} < F_{trip} < 2W_{ac}$
	$\sigma < \sigma_{yield}$

The objective of the optimization is to find the optimal solution for UAS extended reconnaissance by varying the geometry of a gripping mechanism design to produce enough gripping force to carry the weight of the aircraft with minimal tripping force. As stated, this is a single discipline multi-objective design problem that minimizes frontal area, weight, and tripping force while maximizing gripping force by varying the gripper design geometry.

$$\boldsymbol{J} = \min \{W_g, S_g, F_{trip}, -F_{grip}\} \tag{6.1}$$

As discussed in the design trade study in section 4.2.5, the designs cannot be scrutinized from a single discipline. This may be a structural problem, but it has a significant aerodynamic impact as well. For this reason, the single discipline multi-objective design problem is defined to be a multi-disciplinary multi-objective design problem. The new multi-disciplinary objective function would seek to minimize drag and tripping force while maximizing gripping force, rather than minimizing mass, frontal area, and tripping force while maximizing gripping force. This adjustment

to the objective function definition allows aerodynamic and structural inferences to be made when comparing the different concepts in the defined design space. Hence, the new setup for the design problem is defined in terms of the objective function stated in equation 6.2.

$$\boldsymbol{J} = \min \{D_g(W_g, S_g), F_{trip}, -F_{grip}\} \tag{6.2}$$

The *MATLAB surrogate modeling toolbox* is used for implementation of EGO and it applies a *single*-objective design optimization scheme. Therefore, an objective cost function is defined using the penalty method and the method of weighted sums to enforce the constraints of the design problem, described in section 1.3. The *multi*-disciplinary objective function, equation 6.2, is reduced to define the objective statement, equation 6.1 as a *single*-objective cost function,

$$J_C = \min C(D_g(W_g, S_g), \delta^{\sigma}_{F_{grip}}, \delta^{0}_{F_{trip}}, \delta^{+}_{F_{grip}}, \delta^{-}_{F_{grip}}, \delta^{F}_{F_{grip}}, , \delta^{0}_{F_{trip}}, \delta^{+}_{F_{trip}}, \delta^{-}_{F_{trip}}) \tag{6.3}$$

where the cost is defined as sum of the objective statement and the constraint applied via penalty method and the method of weighted sums. in equation 6.4.

$$\begin{aligned} C = D_g(W_g, S_g) + \lambda_1\delta_{\sigma} + w_1\delta^{0}_{F_{grip}} + \lambda_1\delta^{+}_{F_{grip}} + \\ + \lambda_1\delta^{-}_{F_{grip}} + w_2\delta^{F}_{F_{grip}} + w_1\delta^{0}_{F_{trip}} + \lambda_1\delta^{+}_{F_{trip}} + \lambda_1\delta^{-}_{F_{trip}}. \end{aligned} \tag{6.4}$$

Recall in section 1.3, the aircraft drag is subtracted from the total drag to yield the total drag due to the gripping mechanism, D_g. In equation 6.5 the terms that remain represent the induced drag on the aircraft due to the additional weight of the gripping mechanism and the profile drag due to the frontal area of the gripping mechanism.

$$D_g = D - D^0_{ac} = \frac{2W_{ac}S_{ac}}{q_{\infty}S_w^2\pi AR}W_g + \frac{S_{ac}}{q_{\infty}S_w^2\pi AR}W_g^2 + C_{D_g}S_g q_{\infty} \tag{6.5}$$

Thus, equation 6.4, as applied in the optimizer, is represented as follows.

$$C = \alpha W_g + \beta W_g^2 + \gamma S_g + \lambda_1 \delta_\sigma + w_1 \delta^0_{F_{grip}} + \lambda_1 \delta^+_{F_{grip}} + \\ + \lambda_1 \delta^-_{F_{grip}} + w_2 \delta^F_{F_{grip}} + w_1 \delta^0_{F_{trip}} + \lambda_1 \delta^+_{F_{trip}} + \lambda_1 \delta^-_{F_{trip}} \quad (6.6)$$

Notice that the weight coefficients, $\alpha, \beta,$ and γ, in equation 6.4 do not require assumptions and tuning in the final objective cost function. Rather, the weights are analytically resolved as the coefficients of the gripper weight and frontal area in the drag equation, equation 6.5. The following section, section 6.2.1, will describe the method of weighted sums and the penalty method as well as their respective jurisdictions within the same design space.

6.2.1 Optimization Constraints

In this work, the optimization will implement both the method of weighted sums and the penalty method to fully capture the desired behavior of the gripper for the extended reconnaissance missions. The different jurisdictions of the methods are depicted in Figure 6.1 in the gripping force verses tripping force design space. The red shaded areas represent the maximum and minimum tripping penalties and the blue represents the maximum and minimum gripping force penalties for the gripper designs. In some cases, more than one penalty can be applied simultaneously. These overlapping penalties are represented by the purple shaded regions. The different regions represent different violations that will be implemented using two different methods:

1. Penalty Method

   The penalty method is implemented for each constraint violation of the design problem. As seen in Figure 6.1, the objective cost function is subjected to the penalty method when one or more of the constraints are violated. In some cases as depicted by the purple quadrants, more than one penalty may be applied in cases when more than one constraint is violated. Each constraint, $\delta^\sigma_{F_{grip}}, \delta^+_{F_{grip}}, \delta^-_{F_{grip}}, \delta^F_{F_{grip}}, \delta^+_{F_{trip}},$ and $\delta^-_{F_{trip}}$, is associated with a corresponding penalty coefficient, $\lambda_1 = 0.1$, that is multiplied by the violation constraints.

2. Method of Weighted Sums

   The method of weighted sums is applied when the tripping and gripping force constraints are not violated but addition information that the penalty cannot relay needs to be communicated. This method is implemented for the tripping force minimization constraint, the gripping force maximization constraint and the failed run constraint, denoted by $\delta^0_{F_{grip}}$, $\delta^0_{F_{trip}}$, and $\delta^F_{F_{grip}}$, subjected to weights, $w_1 = 0.1$ and $w_2 = 0.1$ respectively. This is necessary to lead the optimizer to maximize gripping force and minimize tripping force within the constraint ranges of the design problem. The goal is to find the closest possible solution to the Utopia point represented by the red star in Figure 6.1. Therefore, when inside the constraints box, created by the minima and maxima of the tripping and gripping force constraints, the optimizer must maximize gripping force and minimize tripping force.

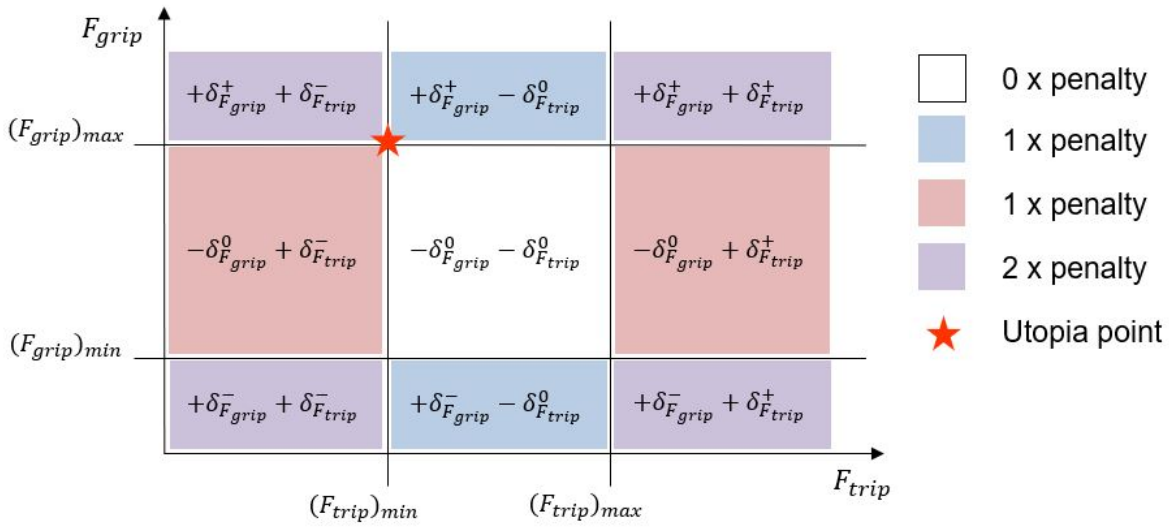

Figure 6.1: Design optimization constraint box.

In addition to constraints, the optimization in this work will subject all output variables (e.g., gripping force, tripping force, maximum von Mises Stress...) to a safety factor of 1.2 before applying constraints. This section will describe these constraints and their corresponding penalties or weights as implemented in equation 6.6.

6.2.1.1 Maximum von Mises Stress Constraint

When maximum von Mises stress, σ, exceeds the yield strength, σ_{yield}, of the material, cost is penalized via the penalty method described in Figure 6.1, and section 6.2.1. The maximum von Mises stress is normalized with respect to the yield strength of the material. As the maximum normalized von Mises stress exceeds the yield strength of the material the penalty increases quadratically. A safety factor of 1.2 is applied to the maximum von Mises stress of the material by comparing the normalized stress with the failure factor of $1/SF$.

$$\delta_\sigma = \begin{cases} (\frac{\sigma}{\sigma_y} - \frac{1}{SF})^2 & \text{if } \sigma > \sigma_{yield} \\ 0 & \text{if } \sigma < \sigma_{yield} \end{cases} \tag{6.7}$$

6.2.1.2 Maximum and Minimum Gripping Force Constraint

The maximum gripping force requires the application of two different methods as mentioned in section 6.2.1. The constraint in question is re-stated below for the following discussion.

$$(F_{grip})_{min} < F_{grip}/SF < (F_{grip})_{max}$$

$$W_{ac} < F_{grip}/SF < 4W_{ac}$$

For the DOE in this work, over 80% of the designs run to completion. The remaining 20% fail, because the quasi-static solver does not reduce the time step enough to capture the high speed dynamic "impact" of the gripper when the reaction moments become large enough. As a result, the analysis fails and the post processors returns a gripping force of zero. Therefore, a constraint has been applied to the cost function by method of weighted sums. The weight of the constraint is defined as $w_2 = 0.001$. This tells the optimizer to add a weight of 0.001, to negatively affect cost.

A unique constraint for the situation is necessary, represented by equation 6.8, because the designs do not fail due in-feasibility. They fail due to the selected solver and it is important to communicate to the optimizer that the selected inputs are not necessarily infeasible. Had we ap-

plied the penalty method just as the other constraints, we risk communicating incorrect information to the optimizer and updating the surrogate incorrectly.

$$\delta^{F}_{F_{grip}} = \begin{cases} 1 & \text{if } F_{grip} = 0 \\ 0 & \text{else} \end{cases} \tag{6.8}$$

When the gripping force violates constraints, the penalty method is applied to the objective statement by quadratically adding the normalized difference between the value of gripping force and the value of the constraint bound that has been violated. The penalty method for the minimum and maximum bounds of the gripping force is represent by equations 6.9 and 6.10.

$$\delta^{-}_{F_{grip}} = \begin{cases} (\frac{(F_{grip})_{min} - F_{grip}}{F_{grip}})^2 & \text{if } (F_{grip})_{min} > F_{grip} \\ 0 & \text{else} \end{cases} \tag{6.9}$$

$$\delta^{+}_{F_{grip}} = \begin{cases} (\frac{F_{grip} - (F_{grip})_{max}}{(F_{grip})_{max}})^2 & \text{if } F_{grip} < (F_{grip})_{max} \\ 0 & \text{else} \end{cases} \tag{6.10}$$

The maximum and minimum constraints are not enough to lead the optimizer towards the approximate optimal design in the design space. In order to communicate to the optimizer that within the constraint the gripping force must be maximized, the method of weighted sums is applied to the gripping force when the constraints are not violated. The method applies a weight coefficient of $w_1 = 0.1$ to the normalized difference between the value of the minimum constraint and the gripping force of the design. This normalized difference is then multiplied by the weight and subtracted from the cost. With an optimization function that minimizes the cost, subtracting cost rewards the optimizer and encourages it to search for designs that are further away from the value of the minimum constraint. This reward scheme is represented by equation 6.11.

$$\delta^0_{F_{grip}} = \begin{cases} -(\frac{F_{grip}-(F_{grip})_{min}}{(F_{grip})_{min}}) & \text{if } (F_{grip})_{min} < F_{grip} < (F_{grip})_{max} \\ 0 & \text{else} \end{cases} \tag{6.11}$$

6.2.1.3 Maximum and Minimum Tripping Force Constraint

Similar to gripping force from subsection 6.2.1.2, the maximum tripping force requires the application of two different constraint methods. The constraint in question is re-stated below for the following discussion.

$$(F_{trip})_{min} < F_{trip}/SF < (F_{trip})_{max}$$

$$W_{ac}/2 < F_{trip}/SF < 2W_{ac}$$

When the tripping force violates constraints, the penalty method is applied to the objective statement by adding the normalized quadratic difference between the value of gripping force and constraint value that has been violated. The penalty method for the minimum and maximum bounds of the tripping force is represent by equations 6.12 and 6.13.

$$\delta^-_{F_{trip}} = \begin{cases} (\frac{(F_{trip})_{min}-F_{trip}}{F_{trip}})^2 & \text{if } (F_{trip})_{min} < F_{trip} \\ 0 & \text{else} \end{cases} \tag{6.12}$$

$$\delta^+_{F_{trip}} = \begin{cases} (\frac{F_{trip}-(F_{trip})_{max}}{(F_{trip})_{max}})^2 & \text{if } F_{trip} > (F_{trip})_{max} \\ 0 & \text{else} \end{cases} \tag{6.13}$$

As when gripping force does not violate constraint, the optimizer is rewarded. However, in optimizer is rewarded for minimizing the tripping force within the constraints. The method applies a weight coefficient of $w_1 = 0.1$ to the normalized difference between the value of the maximum constraint and the tripping force of the design. This normalized difference is then multiplied by the weight and subtracted from the cost. Thus, the optimizer is encouraged to search for designs

that are further away from the maximum constraint value. This reward scheme is represented by equation 6.14.

$$\delta^0_{F_{trip}} = \begin{cases} -(\frac{(F_{trip})_{max} - F_{trip}}{(F_{trip})_{max}}) & \text{if } (F_{trip})_{min} < F_{trip} < (F_{trip})_{max} \\ 0 & \text{else} \end{cases} \tag{6.14}$$

6.3 Final Gripper Design

After the optimization is complete, the LP design with the lowest cost per the objective cost statement defined in equation 6.3 is chosen as to be the final optimal solution for the extended reconnaissance mission. In Figure 6.3 we can see that the optimization did indeed find a lower cost gripper design. It is important to note that the optimization was performed using Markforged Onyx material properties and quasi-static time integration.

The results of the DOE and the optimization confirm that the objective cost statement works and that an approximate global minimum has been reached within the defined object space. Upon examining the best designs of the DOE and the optimization, it is clear that the optimal solution was reached despite not having reached the maximum and minimum of the gripping and tripping force constraints respectively. This can inferred due to the slight increase in gripper drag for the best optimization design when compared with the DOE best design. As suspected, there is trade off between higher forces and lowering mass and frontal area.

Best Design	Tripping Force (N)	Gripping Force (N)	Gripper Drag (N)
DOE	25	28	0.04
Optimization	20	70	0.07

Table 6.1: Low profile model final design comparison.

Therefore, the final gripper design can be claimed as the optimal design within the constraints of the given problems and with the small initial sample size of the LHS DOE.

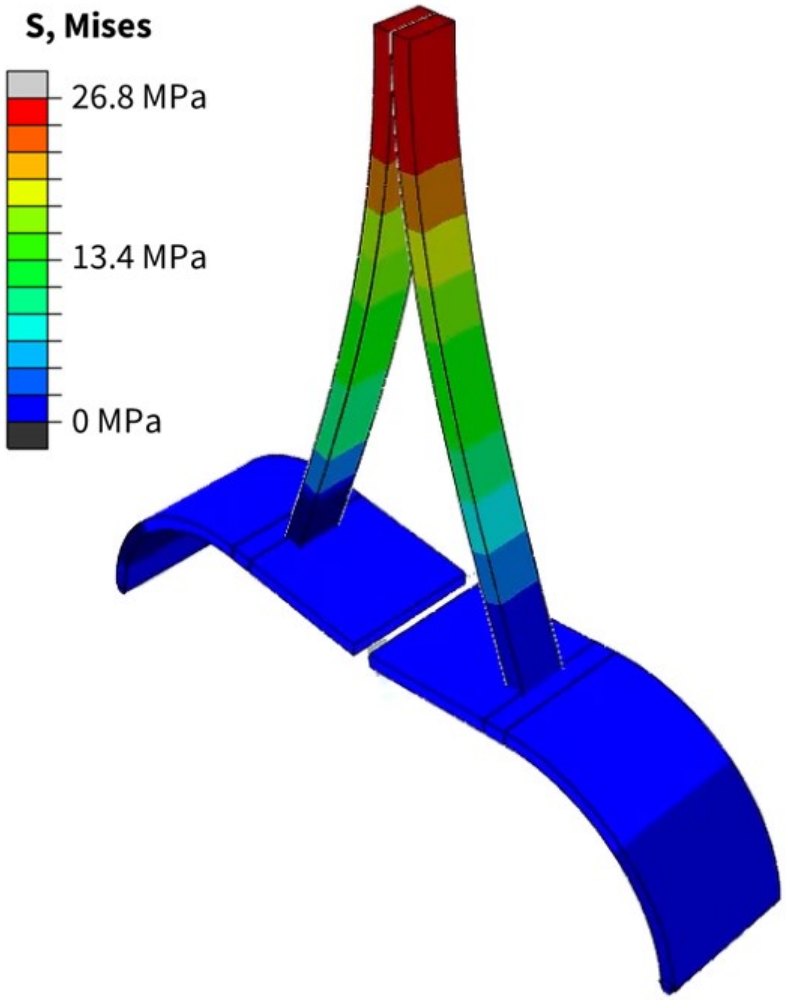

Figure 6.2: LP Optimization Final Result.

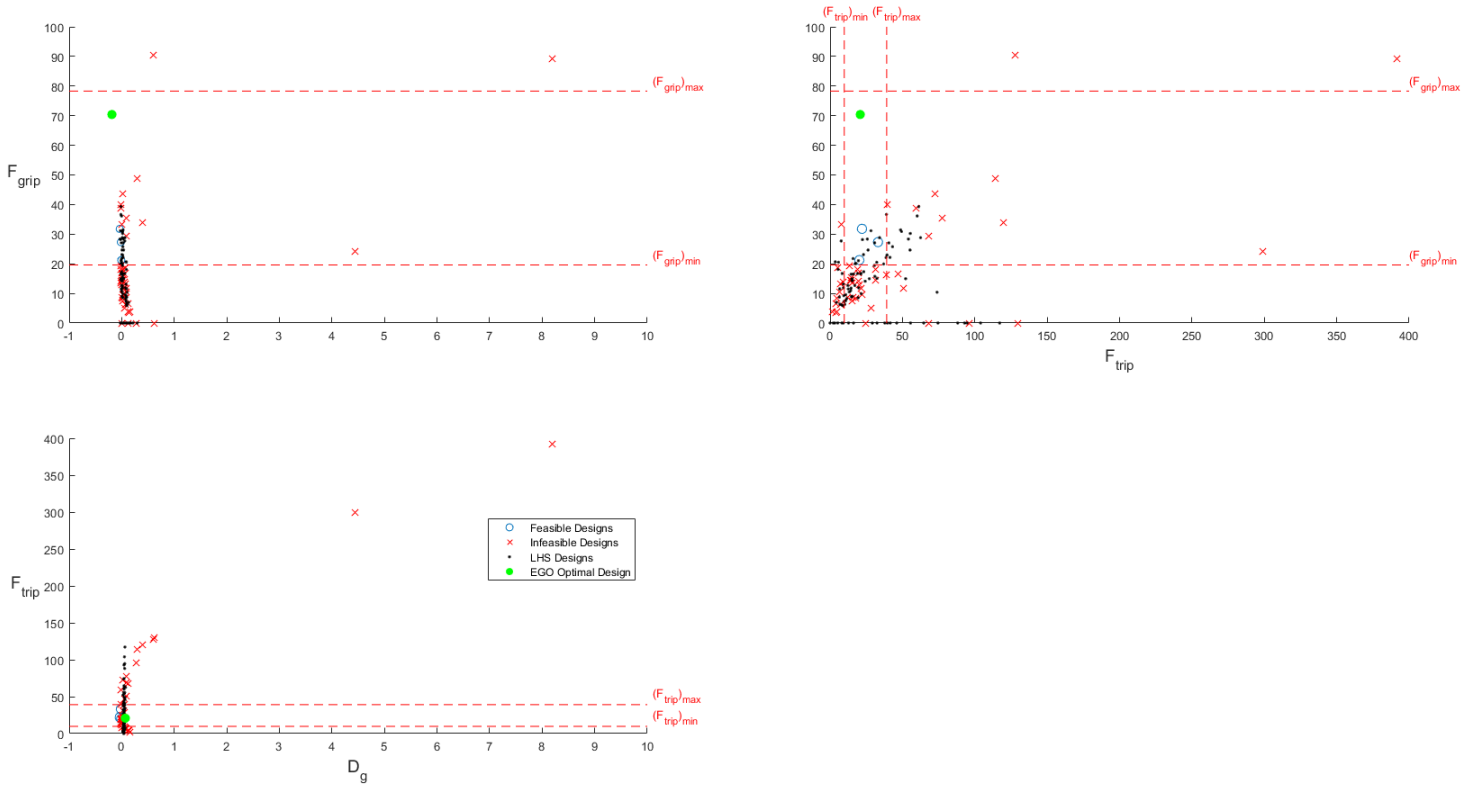

Figure 6.3: Low profile optimization.

REFERENCES

[1] J. A. V. N. T. S. C. (U.S.), "Unmanned Aircraft System (UAS) service demand 2015 - 2035 : literature review & projections of future usage, technical report, version 1.0 - February 2014," 2 2014.

[2] G. V. Bogel, L. Cousin, N. Iversen, E. S. M. Ebeid, and A. Hennig, "Drones for Inspection of Overhead Power Lines with Recharge Function," *Proceedings - Euromicro Conference on Digital System Design, DSD 2020*, pp. 497–502, 8 2020.

[3] N. Iversen, O. B. Schofield, L. Cousin, N. Ayoub, G. Vom Bogel, and E. Ebeid, "Design, Integration and Implementation of an Intelligent and Self-recharging Drone System for Autonomous Power line Inspection," *IEEE International Conference on Intelligent Robots and Systems*, pp. 4168–4175, 2021.

[4] H. T. Hsiao, J. Sun, H. Zhang, and J. Zhao, "A Mechanically Intelligent and Passive Gripper for Aerial Perching and Grasping," *IEEE/ASME Transactions on Mechatronics*, vol. 27, pp. 5243–5253, 12 2022.

[5] A. E. Gomez-Tamm, V. Perez-Sanchez, B. C. Arrue, and A. Ollero, "SMA actuated low-weight bio-inspired claws for grasping and perching using flapping wing aerial systems," *IEEE International Conference on Intelligent Robots and Systems*, pp. 8807–8814, 10 2020.

[6] A. McLaren, Z. Fitzgerald, G. Gao, and M. Liarokapis, "A Passive Closing, Tendon Driven, Adaptive Robot Hand for Ultra-Fast, Aerial Grasping and Perching," *IEEE International Conference on Intelligent Robots and Systems*, pp. 5602–5607, 11 2019.

[7] Y. Zhu, X. He, P. Zhang, G. Guo, and X. Zhang, "Perching and Grasping Mechanism Inspired by a Bird's Claw," *Machines*, vol. 10, p. 656, 8 2022.

[8] Aerovironment, "RAVEN B RQ-11 data sheet," 2022.

[9] "Frog Grabber– H&H Lure Company."

[10] N. G. Odneal, “Frog gaff,” U.S. Patent 2 616 753, Nov. 1952.

[11] *Abaqus Documentation*. Dassault Systemes, 2021.

[12] Marekforged, “Composites material data sheet,” 2022.

[13] J. Müller, “MATSuMoTo: The MATLAB Surrogate Model Toolbox For Computationally Expensive Black-Box Global Optimization Problems,” 4 2014.

[14] S. P. Nevin, J. E. El-Ashkar, C. N. Gillaspie, and D. J. Hartl, “Shape Memory Alloys for Regulating TCS in Space (SMARTS): Validated Multiphysical Modeling and Design Optimization of Morphing Composite Radiators,” 2022.

[15] G. Wilson, “Shaping Radiation Contours with a Parabolic Active Reconfigurable Origami Reflector Antenna,” 2020.

[16] P. A. J. K. Dr Alexander I. J. Forrester, Dr András Sóbester, “Constructing a Surrogate,” in *Engineering Design via Surrogate Modelling*, ch. 2, pp. 33–76, John Wiley & Sons, Ltd, 2008.

[17] D. R. Jones, M. Schonlau, and W. J. Welch, “Efficient Global Optimization of Expensive Black-Box Functions,” *Journal of Global Optimization*, vol. 13, no. 4, pp. 455–492, 1998.